



# Modeling of rupture using strong motion generation area: a case study of Hualien earthquake ( $M_w$ 6.1) occurred on April 18, 2019

Saurabh Sharma<sup>1</sup> · Anand Joshi<sup>1</sup> · Sandeep<sup>2</sup> · Che-Min Lin<sup>3</sup> · Chun-Hsiang Kuo<sup>4</sup> · Kuo-Liang Wen<sup>4</sup> · Sandeep Singh<sup>1</sup> · Mukat Lal Sharma<sup>5</sup> · Mohit Pandey<sup>1</sup> · Jyoti Singh<sup>1</sup>

Received: 9 January 2022 / Accepted: 29 July 2022 / Published online: 19 September 2022

© The Author(s) under exclusive licence to Institute of Geophysics, Polish Academy of Sciences & Polish Academy of Sciences 2022

## Abstract

The strong Hualien earthquake ( $M_w$  6.1) occurred along the suture zone of the Eurasian Plate and the Philippine Sea Plate, which struck the Hualien city in eastern Taiwan on April 18, 2019. The focal mechanism of this earthquake shows that it is caused by a rupture within a thrust. In the present study, the rupture plane responsible for this earthquake has been modeled using the modified semi-empirical technique (MSET). The whole rupture plane is assumed to be composed of strong motion generation areas (SMGAs) along which the slip occurs with large velocities. The spatiotemporal distribution of aftershocks of this earthquake within identified rupture plane suggests that there are two SMGAs within the rupture plane. The source displacement spectra (SDS) obtained from the observed records have been used to compute the source parameters of these two SMGAs. The MSET efficiently simulates strong ground motion (SGM) at the rock site. The shallow subsurface shear wave velocity profile at various stations has been used as an input to SHAKE91 algorithm for converting records at the surface to that at the rock site. The simulated records are compared with the observed records based on root-mean-square error (RMSE) in peak ground acceleration (PGA) of horizontal components. Various parameters of the rupture plane have been selected using an iterative forward modeling scheme. The accelerograms have been simulated for all the stations that lie within an epicentral distance ranging from 5 to 100 km using the final rupture plane parameters. The comparison of observed and synthetic records validates the effectiveness of the simulation technique and suggests that the Hualien earthquake consists of two SMGAs responsible for high-frequency SGM.

**Keywords** 2019 Hualien earthquake · Modified semi-empirical technique · Strong motion generation area

---

Edited by Dr. Aybige Akinci (ASSOCIATE EDITOR) / Prof. Ramón Zúñiga (CO-EDITOR-IN-CHIEF).

✉ Saurabh Sharma  
ssharma1@es.iitr.ac.in

<sup>1</sup> Department of Earth Sciences, Indian Institute of Technology Roorkee, Roorkee, India

<sup>2</sup> Department of Geophysics, Institute of Science, Banaras Hindu University, Varanasi, India

<sup>3</sup> National Center for Research on Earthquake Engineering, Taipei, Taiwan

<sup>4</sup> Department of Earth Sciences, National Central University, Taoyuan City, Taiwan

<sup>5</sup> Department of Earthquake Engineering, Indian Institute of Technology Roorkee, Roorkee, India

## Introduction

Strong ground motion (SGM) is the strong earthquake shaking that occurs close to a causative fault. The strength of shaking involved in SGM usually overwhelms a seismometer, forcing the use of accelerographs for recording strong ground motion at both near and far-field stations. SGM is an integral component of earthquake-resistant design criteria. The SGM simulation can be done by several techniques. The oldest simulation technique is the stochastic simulation technique that was initially proposed by Boore (1983) to simulate the SGM of high frequency. Hanks and McGuire (1981) utilized a white Gaussian noise carrying the lowest frequency known as corner frequency  $f_o$ , and the highest frequency  $f_{max}$  to estimate the SGM. This process initiates with the generation of white Gaussian noise, which acts as an input for the time-domain shaping taper to match the shape of the envelope of the expected SGM. Then, the Fourier transform is applied to transform it into the frequency domain. Finally, to match the anticipated spectral shape, it is further passed through a band-pass filter (Erdik and Durukal 2004). This simulation method is used by Toro and McGuire (1987) and Atkinson and Boore (1995). The finite source stochastic model's major drawback is its dependency on the number, or the size of the sub-faults used in the simulation (Joyner and Boore, 1986).

Miyake et al. (2003) demonstrated that some patches within the rupture plane are mainly responsible for high-frequency SGM known as strong ground-motion areas (SMGAs). The high velocity of slip delineates these SMGAs, which are used to model the entire fault plane. Miyake et al. (2003) incorporated the SMGAs into the technique to model the Yamaguchi earthquake ( $M_w = 5.9$ ) of 1997, the Kagoshima earthquake ( $M_w = 6.1$ ) of 1997, and Iwate earthquake ( $M_w = 6.1$ ) of 1998. Miyahara and Sasatani (2004), and Takiguchi et al. (2011) implemented the impact of SMGAs in Empirical Green's function (EGF) technique to study the source model of an earthquake.

The different-sized sub-events can describe the complex rupture process during earthquakes. These sub-events constitute a composite source model used by Frankel (1991), Zeng et al. (1994), and Yu et al. (1995). In this technique, the source model's complexity is assumed, according to which randomly distributed sub-events of constant stress drop in the entire fault plane constitute a mainshock. The radiation from each sub-event takes the shape of Brune (1970) pulse. An appropriate delay is added to each sub-event. The summing of the independent source-time function results in the high-frequency radiation of the mainshock. Finally, SGM simulation is achieved when the convolution is applied between the composite source generated from the contribution from all sub-events and the synthetic Green's functions. The reliability of this technique for the generation of realistic time histories has been confirmed by Zeng et al. (1994). The main limitation of this method lies in the requirement of the Q-structure of the region, source mechanism, and velocity structure of the region.

Hartzell (1978) proposed the EGF technique that uses the records of small magnitude earthquakes that occur in the vicinity of mainshock as EGF. The aftershocks and foreshocks of the mainshock can be used as small magnitude earthquakes. They can be approximated as a point source on the fault for the large target earthquake. The EGFs after being time-delayed and summed approximate the mainshock record. The precision of this methodology was tested by many researchers Kanamori (1979), and Irikura (1983). Irikura (1983) proposed some modifications in Hartzell's approach to calculate the count of sub-events to be used in the summation by taking the ratio of the main event's seismic moment to the sub-event based on the source model of Haskell type and the similarity laws of earthquakes. The SGMs for different world regions have been synthesized using the EGF approach (Irikura et al. 1997; Sharma et al. 2013). EGF approach serves as an effective and authentic simulation technique among the previously discussed SGM simulation methods. The applicability of the EGF technique is limited due to the lack of the desired signal-to-noise ratio, difference in the source mechanism of the target event, and

**Table 1** Mainshock parameters of the 2019 Hualien earthquake. The parameters  $\lambda$ ,  $\phi_s$ , and  $\delta$  represent the rake, strike, and dip, respectively. NP1 and NP2 are Nodal planes

Origin time	Location	Size	Fault plane solution	Agency
18/04/19 05:01:8.7 (GMT)	24.09°N, 121.40°E Depth = 30 km	$M_o = 2.34 \times 10^{18}$ Nm $M_w = 6.2$	NP1: $\phi_s = 68^\circ$ , $\delta = 40^\circ$ , $\lambda = 128^\circ$ ; NP2: $\phi_s = 202^\circ$ , $\delta = 60^\circ$ , $\lambda = 63^\circ$	Global CMT
18/04/19 05:01:06 (GMT)	24.037°N, 121.65°E Depth = 20 km	$M_o = 1.99 \times 10^{18}$ Nm $M_w = 6.1$	NP1: $\phi_s = 215^\circ$ , $\delta = 46^\circ$ , $\lambda = 70^\circ$ ; NP2: $\phi_s = 63^\circ$ , $\delta = 47^\circ$ , $\lambda = 110^\circ$	USGS

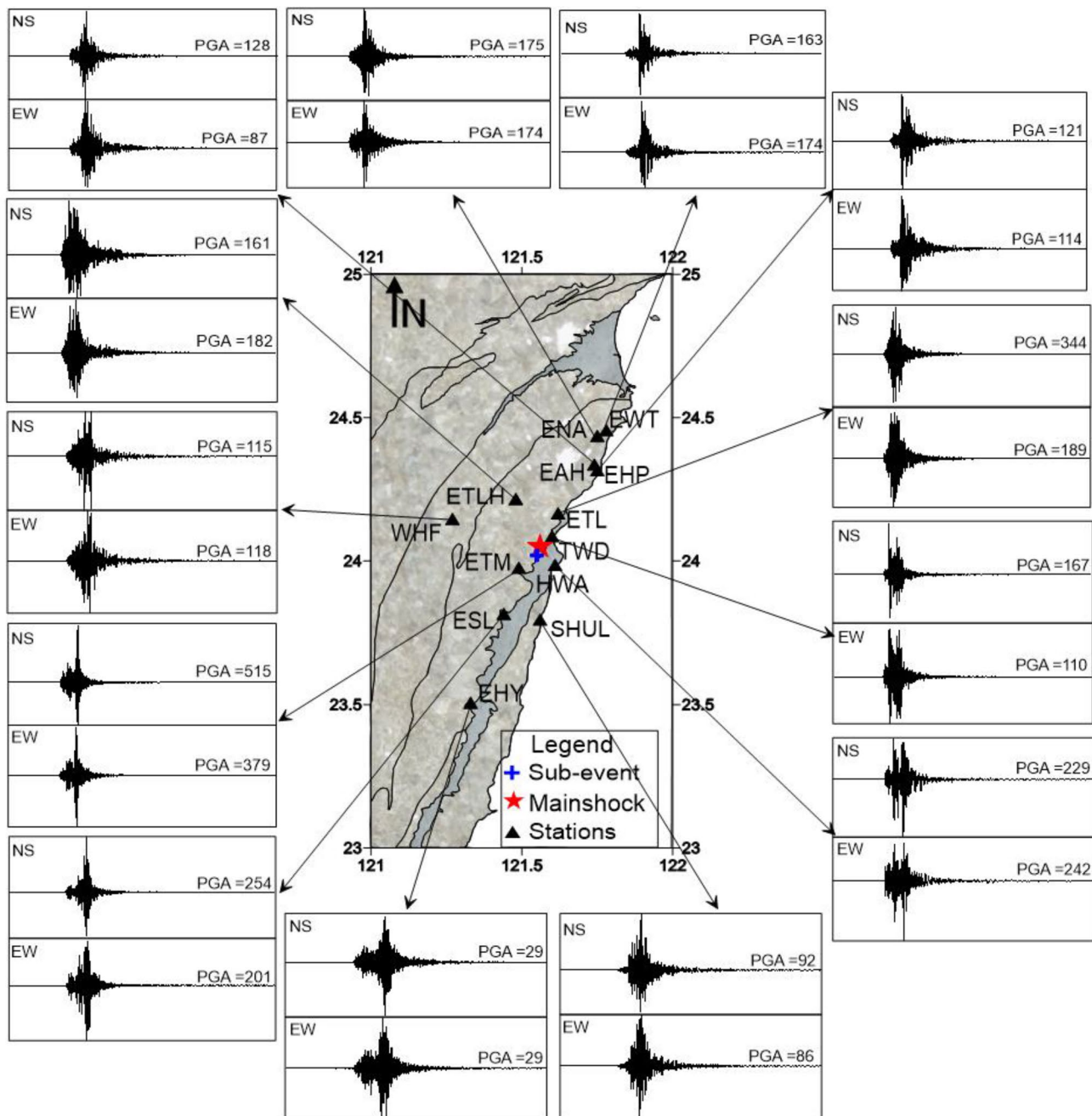


**Fig. 1** Location of stations and the records at surface used for the purpose of simulation of SGM. The unit of PGA is  $\text{cm/s}^2$

Green's function, mainly due to the lack of accessibility of Green's functions at the site of interest.

Midorikawa (1993) proposed the semi-empirical technique (SET) which was modified by Joshi and Midorikawa (2004). The EGF technique proposed by Irikura (1986) is the basis of SET. The SET has been effectively studied by Joshi (1997), Kumar et al. (1999), and Kumar and Khattri (2002) for modeling various Himalayan earthquakes. The stochastic simulation method given by Boore (1983) provides the

time series, and the SET provides the envelope function, which has been combined in the modified semi-empirical technique (MSET) by Joshi et al. (1999), and Kumar and Khattri (2002). The effect of layering in this technique has been included by Joshi (2001), and Joshi and Mohan (2010). The dependency of SET on attenuation relation has been removed by Joshi et al. (2001). A theoretical relation that is based on radiation pattern parameters and the seismic moment has been used to compute peak ground acceleration

**Table 2** Details of the stations and PGA from the recorded data

Stations	Epicentral distance (km)	Vs30 (m/s)	Observed PGA at surface (cm/s <sup>2</sup> )		Observed PGA at rock site (cm/s <sup>2</sup> )	
			(N–S)	(E–W)	(N–S)	(E–W)
TWD	5.5	623	167	110	82	59
ETM	11.9	525	515	379	138	94
ETL	13.2	814	344	189	137	39
ESL	29.3	629	254	201	137	137
EHP	34.0	472	121	114	121	113
EAH	35.5	534	128	87	97	54
ENA	45.4	626	175	174	142	164
EWT	48.6	477	163	174	99	136
EHY	65.3	545	29	29	22	22

**Table 3** Velocity model used in the analysis of source model of this earthquake (Wen et al. 2019)

Depth (km)	Vs (km/s)	Density (kg/m <sup>3</sup> )
3	2.99	2.39
6	3.37	2.57
9	3.44	2.6
15	3.53	2.64
24	3.66	2.66

(PGA). The SET has been modified by Joshi et al. (2012b) for simulating SGM records along N–S and E–W directions. Joshi et al. (2014) modified SET by incorporating the effect of SMGAs. The concept of radiation pattern which is frequency-dependent, has been included by Sandeep et al. (2014a). The MSET has been successfully utilized to model various worldwide earthquakes by Sandeep et al. (2014a, b, and 2019) and Lal et al. (2018).

Recently, eastern part of Taiwan was struck by the Hualien earthquake ( $M_w$  6.1) which occurred on April 18, 2019. The high level of seismicity in Taiwan makes it one of the world's most tectonically active regions. There are various suture zones between the several terranes due to the major faults in Taiwan. Taiwan and the Philippine trench lie near to zone of numerous transform faults. The Philippine Sea

**Table 4** Average values of source parameters obtained from SDS from horizontal components of SMGA1 and SMGA2 at various stations and average values of source parameters of an aftershock computed at TWD station

Event	Corner frequency, $f_c$ (Hz)	Seismic moment, $M_0$ (Nm)	Stress drop, $\Delta\sigma$ ( $\times 10^5$ N/m <sup>2</sup> )
SMGA1	$0.42 \pm 0.004$	$(4.80 \pm 0.98) \times 10^{17}$	$56.10 \pm 14.41$
SMGA2	$0.4 \pm 0.02$	$(5.25 \pm 0.93) \times 10^{17}$	$79.15 \pm 17.27$
Aftershock	$1.71 \pm 0.053$	$2.09 \times 10^{15}$	$23.23 \pm 2.14$

plate (PSP) is moving at the rate of  $\sim 80$  mm/yr with respect to the Eurasian plate (Smoczyk et al. 2013). A suture zone is formed due to Longitudinal Valley (LV) between two plates on land. The Coastal Range lies on the eastern part of LV and is formed by the solidifying andesitic magma and volcanic rocks of the PSP. The Central Range on the LV's western side is a metamorphic terrane of the Eurasian plate. Along the LV, these two plates collide intensively. The southern region of the LV has a relatively less complex structure than the northern region. The Hualien region lies on the north of the LV and is seismically active due to its location in the vicinity of subducting region (Kuo-chen et al. 2004; Wu et al. 2009; Chin et al. 2016; Shyu et al. 2016). The PSP is subducting in the northwest direction in the Hualien region; therefore, two different kinds of earthquake clustering can be spotted based on focal mechanisms: shallow depths (10 km) normal-faulting type due to the PSP bending and shallow-deep depths west-dipping thrust type due to the subduction of the PSP (Kuo-chen et al. 2004).

In the present paper, the MSET is used to simulate the accelerograms at the stations which recorded the Hualien earthquake. The main objective behind the study of this earthquake is to finalize the rupture model of this earthquake and estimate the parameters of SMGAs accountable for this earthquake.

## Data

The Hualien earthquake that occurred on April 18, 2019, was recorded at 107 stations of the Central Weather Bureau (CWB) installed across Taiwan. The accelerograms have been taken from Geophysical Database Management System (GDMS) developed and maintained by CWB. The parameters of the main event have been estimated by different agencies like USGS and Global CMT. The location, size,



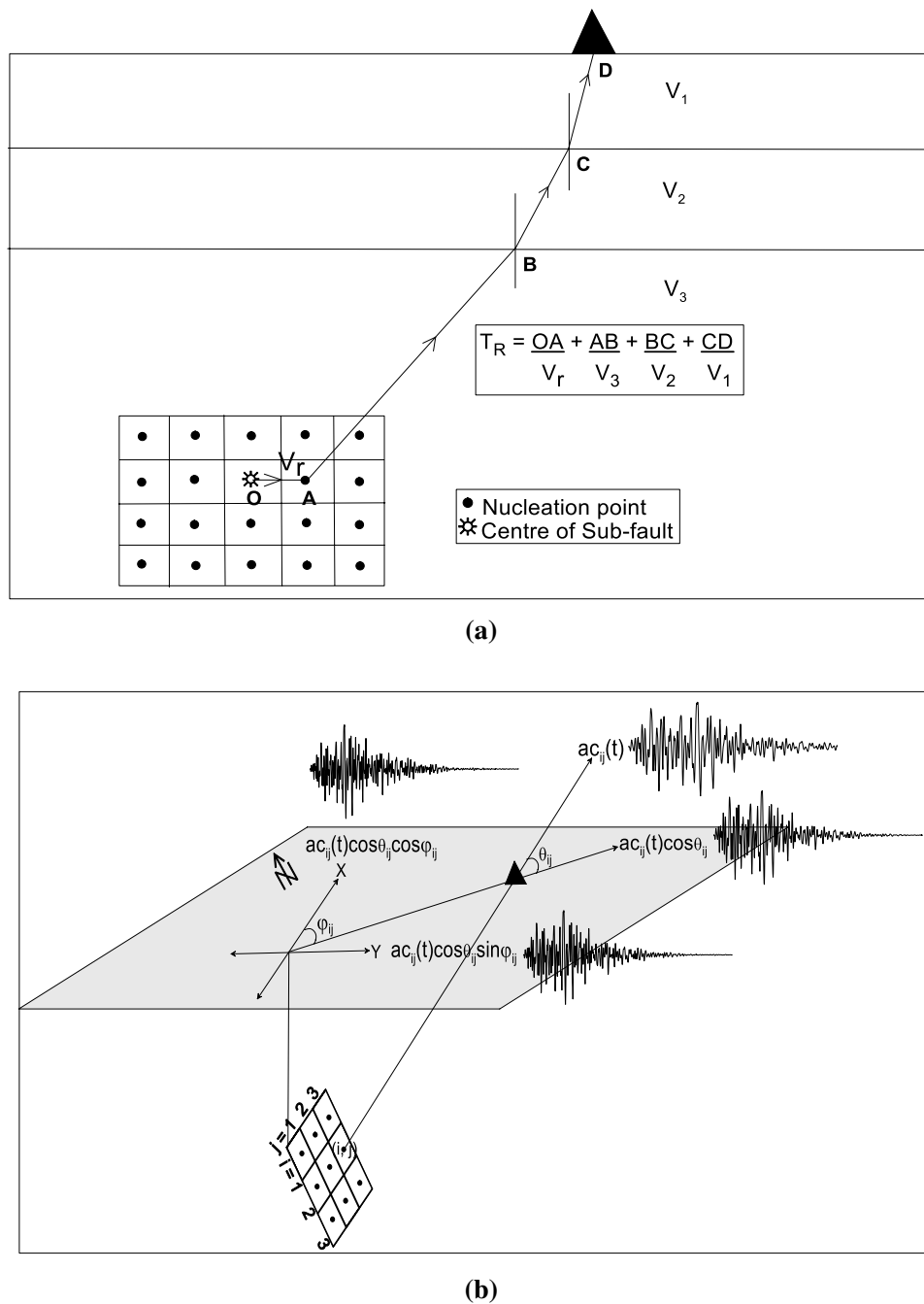


**Fig. 2** (a) Travel time of wave propagation from the nucleation point to recording station at surface and (b) Representation of the procedure used to obtain the horizontal components of ground motion from resultant motion ' $ac_{ij}(t)$ ' due to 'ijth' sub-fault. The (black) triangle specifies the position of the station

and fault plane solution of this earthquake provided by these agencies are given in Table 1.

Recorded data need preliminary processing like baseline correction and instrument correction before being used for the simulation. The simulation data in this research work are already scaled according to the recording sensor, and it is also baseline-corrected. The removal of undesired

frequencies from the recorded data is done using a fourth-order band-pass (0.4–25 Hz) Butterworth filter.

Peak ground acceleration of  $110 \text{ cm/s}^2$  and  $167 \text{ cm/s}^2$  for E–W and N–S components, respectively, has been recorded at station TWD, located at a distance of 6 km from the epicenter as shown in Fig. 1. The maximum PGA of  $379 \text{ cm/s}^2$  and  $515 \text{ cm/s}^2$  for E–W and N–S components,

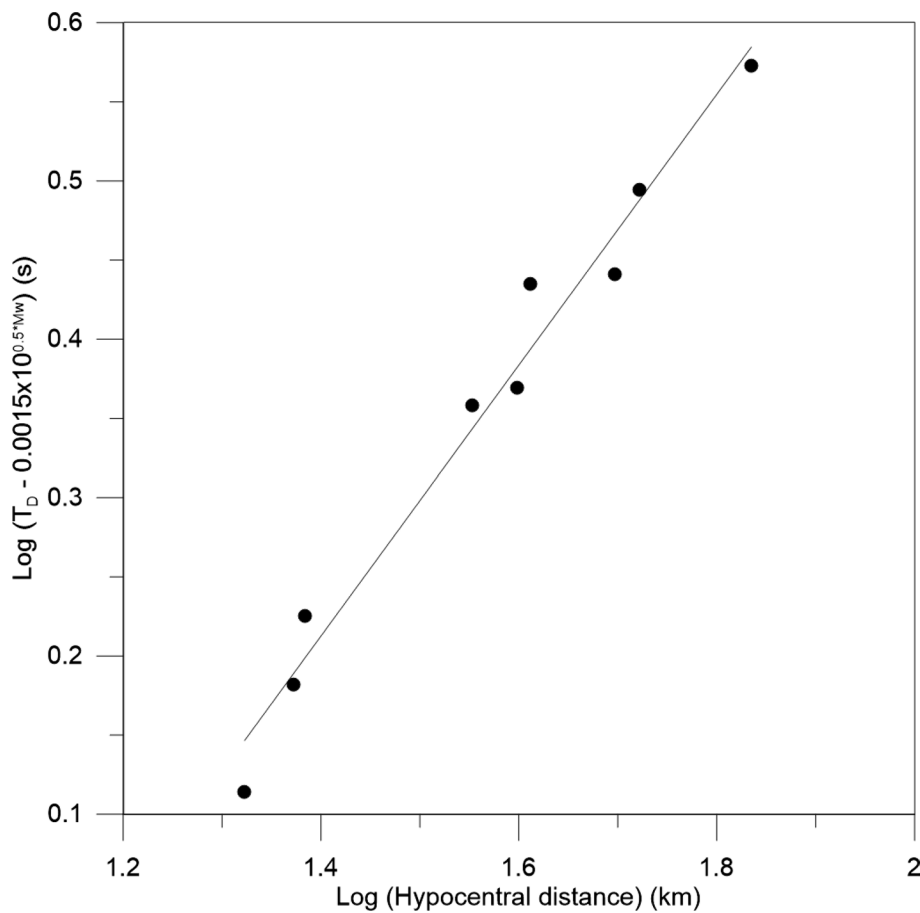


**Fig. 3** Plot to determine the values of coefficients 'a' and 'b' in the regression relation given by Midorikawa (1993)

respectively, is recorded at station ETM, located at a distance of 12 km from the epicenter as shown in Fig. 1. The PGA ( $> 400 \text{ cm/s}^2$ ) is also reported by Mittal et al. (2021). The PGA values between  $25\text{--}80 \text{ cm/s}^2$ , which also corresponds to  $5.7\text{--}17.0 \text{ cm/s}$  PGV contour, have been observed in Taipei which is also reported by Mittal et al. (2021).

The stations that have recorded this earthquake are located mostly at the earth's surface, which consists of site effects due to soil or low-velocity rock mass. Idriss and Sun (1992) provided a FORTRAN code SHAKE91 which is a modified edition of the primary code SHAKE Schnabel et al. (1972) that is derived from the solution to the secondary wave equation (Kanai 1951; Lysmer et al. 1971). This code provides the requisite transfer function for converting records at the surface to bedrock. This algorithm's input is the accelerograms recorded at the stations and the velocity profile of the secondary wave of the subsurface layer. The shear wave velocity at 30 m depth ( $V_{s30}$ ) in Table 2 has been used in the SHAKE91 algorithm to obtain records at the rock site. The processed filtered records have been passed through SHAKE91. The stations used in the present work with the processed record at the surface are shown in Fig. 1.

The PGA obtained at various stations from the records at the surface and the rock site is given in Table 2. The velocity model required in the MSET used in this work is given in Table 3 given by Wen et al. (2019).

## Methodology

The modeling of the rupture plane is based on MSET. In this technique, the scaling laws given by Aki (1967), and Kanamori and Anderson (1975) have been utilized to model the finite rupture source by dividing it into several sub-faults, which act as a single source distributed over a finite rupture plane. The technique can be divided into two parts. Firstly, the acceleration spectra are generated using the criteria given by Boore (1983), and then it is shaped in the frequency domain. The spectral contents of SGM records have been decided based on various filters that depend on parameters like corner frequency of target event, hypocentral distance, frequency-dependent quality factor, and velocity of S-wave of the medium and also on maximum frequency ( $f_{\max}$ ). The process of computing acceleration spectra is based on that

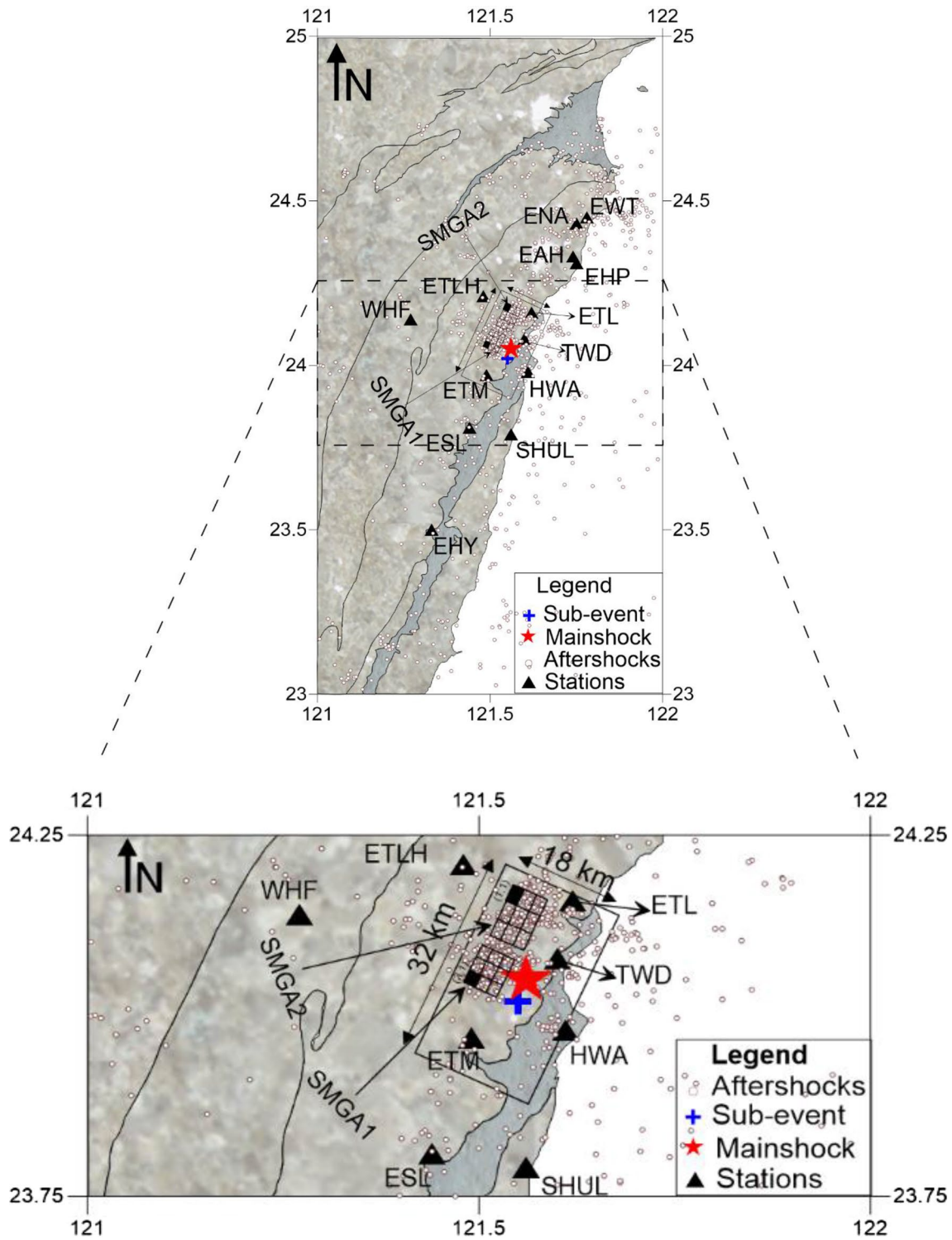


**Fig. 4** Hualien Earthquake source model indicating two SMGAs within the plane of rupture. The red star and solid circles represent the epicenter and aftershocks of this earthquake, respectively

proposed by Boore (1983) and further used by Joshi and Midorikawa (2004) in their SET. Secondly, the time series obtained from the acceleration spectra has been windowed by a deterministic window that depends on the envelope

function (Joshi and Midorikawa 2004). The resultant envelope function is the summation of the envelope function released by different sub-faults at different time lags defined by Midorikawa (1993), Joshi and Midorikawa (2004). The

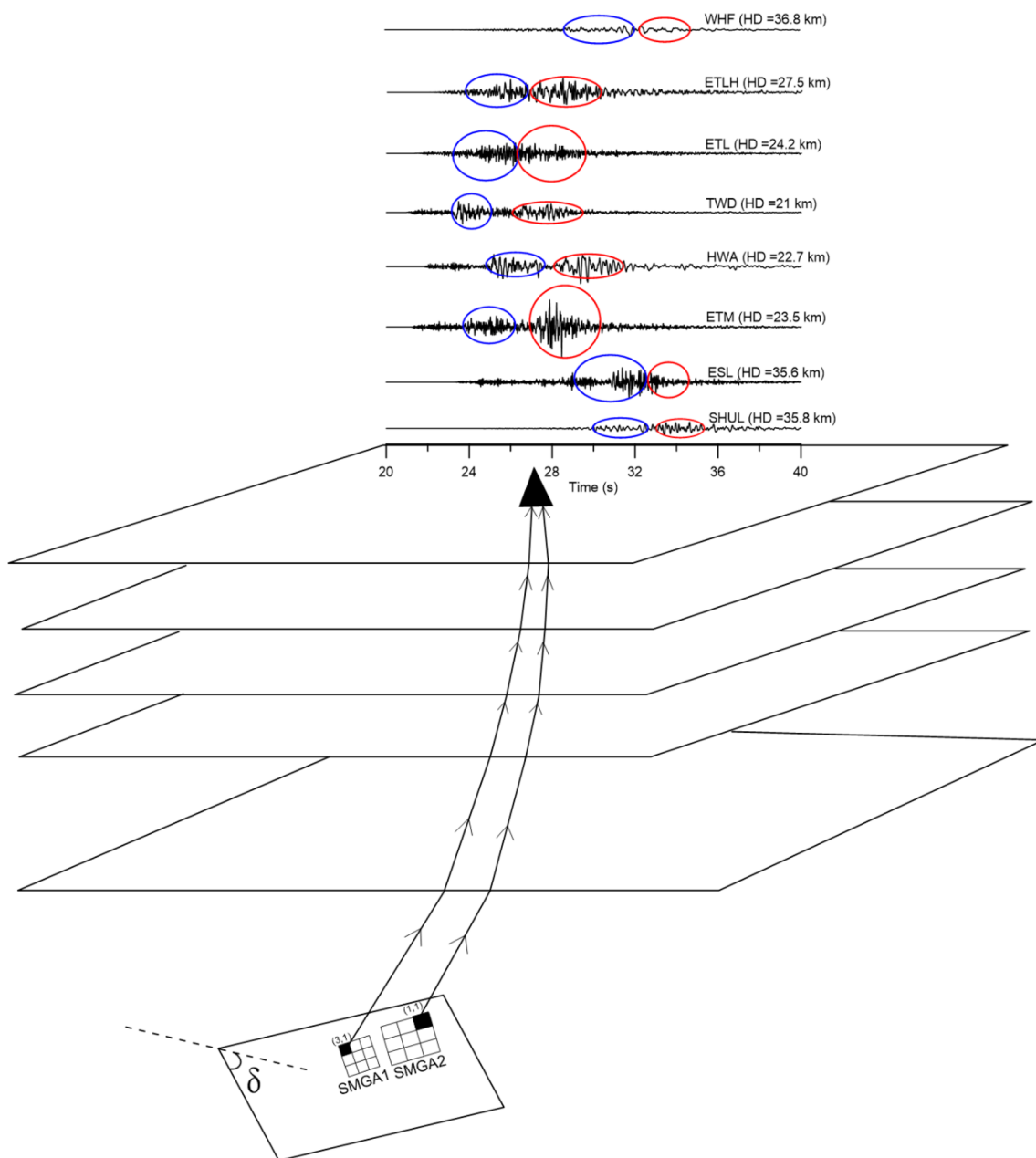


**Fig. 5** Source model of Hualien earthquake in a layered earth medium. Black filled rectangles show the nucleation point of rupture due to identified SMGA. Solid triangle specifies the position of the

station. The waveform contribution from SMGA1 and SMGA2 is shown by the blue and red ellipse, respectively.  $\delta$  denotes the dip of the rupture plane

arrival time of the envelope function at the station depends on the time that the rupture takes to reach the center of the sub-fault from the nucleation point and also on the time which the seismic energy takes to reach the station from the center of sub-faults. The pictorial representation of wave propagation and arrival time calculation is shown in Fig. 2a.

The resultant record has been converted into E–W and N–S components by using the methodology given by Joshi

et al. (2012b). The SMGAs act as a source of energy, and their effects are added appropriately by following the procedure given by Joshi et al. (2014). The radiation of high frequency from SMGAs has been further modeled using the frequency-dependent radiation pattern as used by Sandeep et al. (2014a). The entire procedure of component-wise SGM simulation used in the present work is depicted in Fig. 2b.

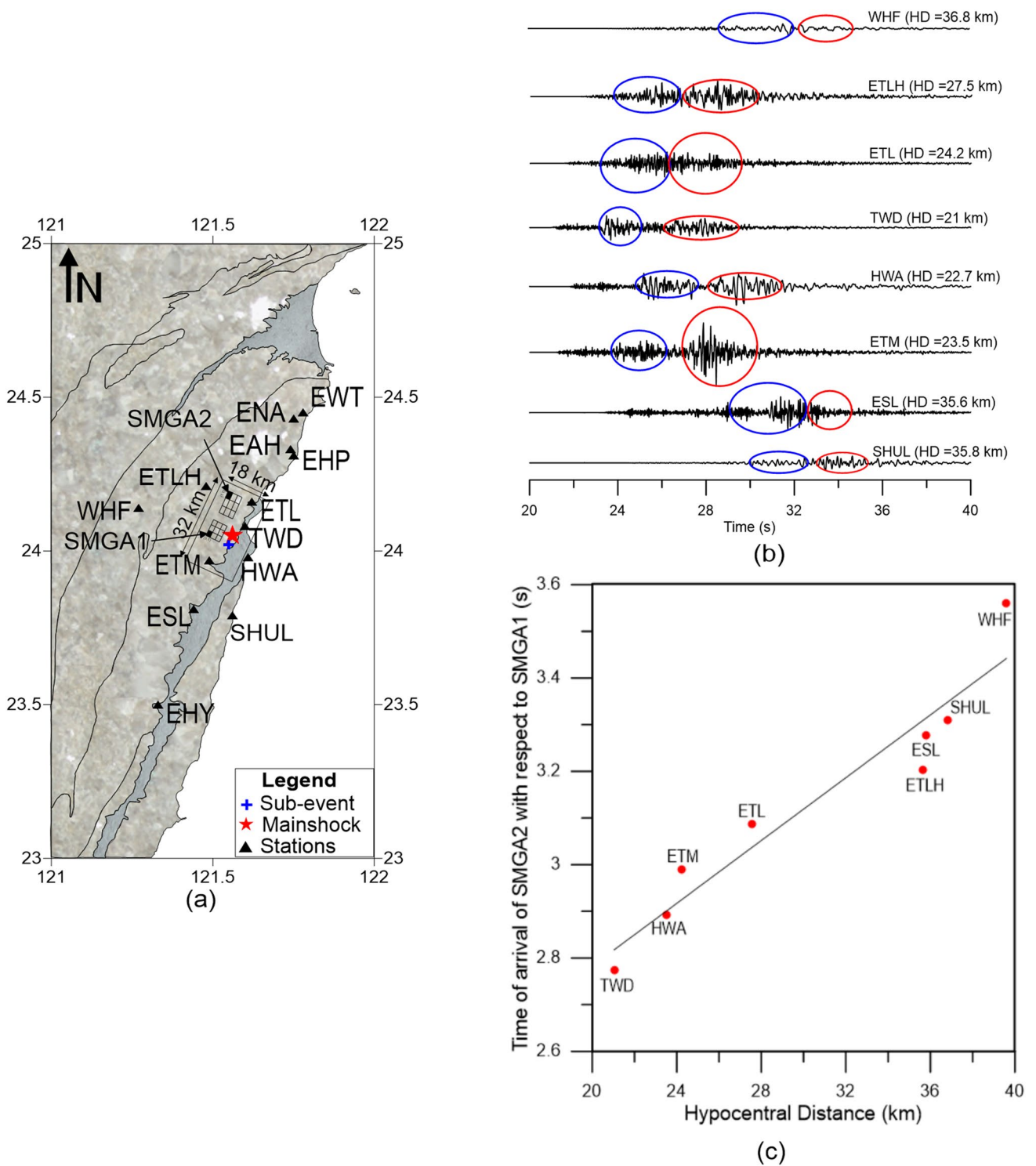


**Fig. 6** **a** Location of stations used to study the time lags between identified SMGAs; **b** The acceleration time series recorded by different stations with phases corresponding to identified SMGAs; **c** Variation of time lags of two SMGAs with respect to the hypocen-

tral distance of recording stations shown in **(b)**. The waveform contribution from SMGA1 and SMGA2 is shown by the blue and red ellipse respectively



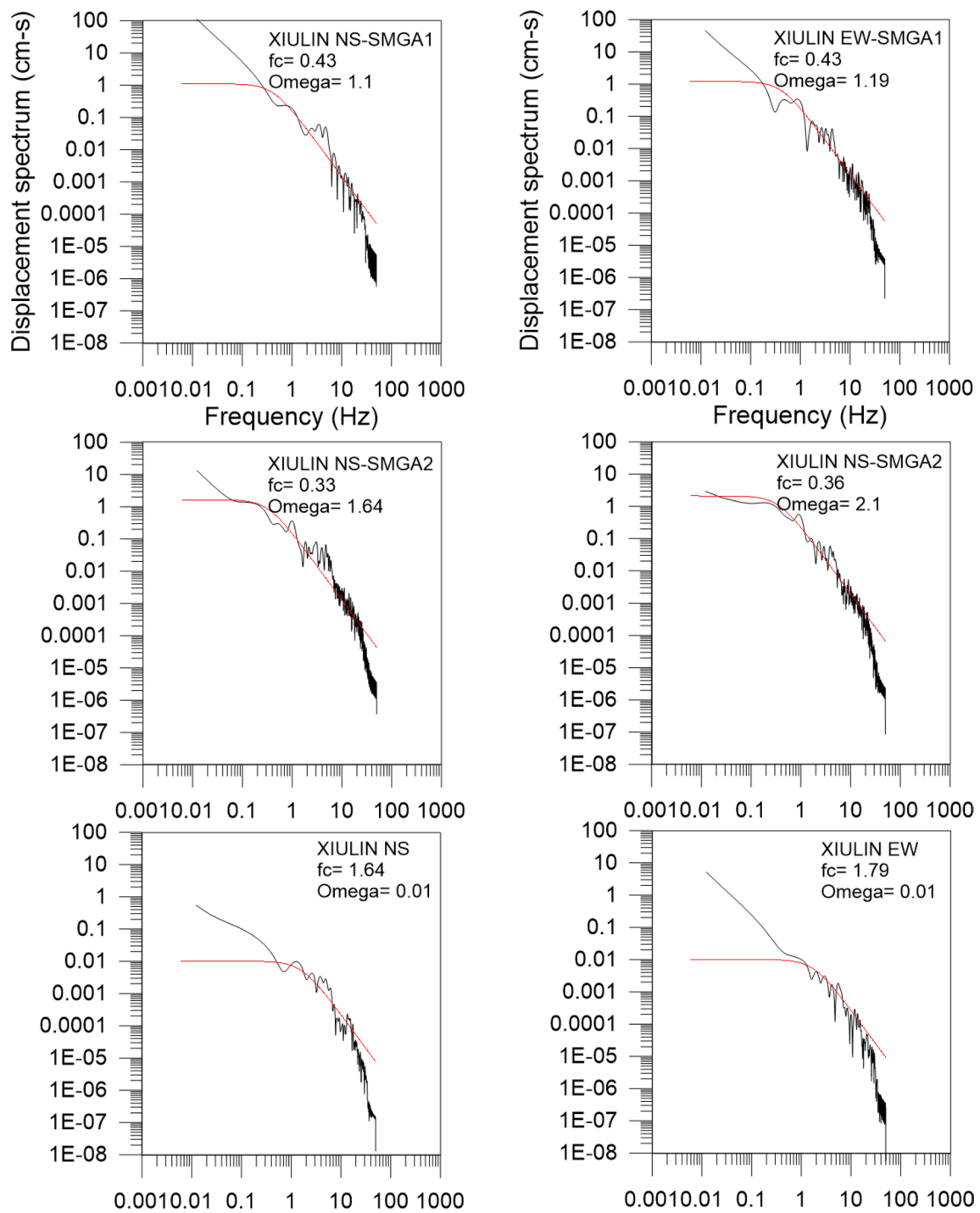


**Fig. 7** SDS obtained from NS and EW components of SMGA1 (black), SMGA2 (black), and aftershock (black) of the Hualien earthquake at TWD station in (a), (b), and (c). Theoretical spectra fit (red) on SDS, respectively

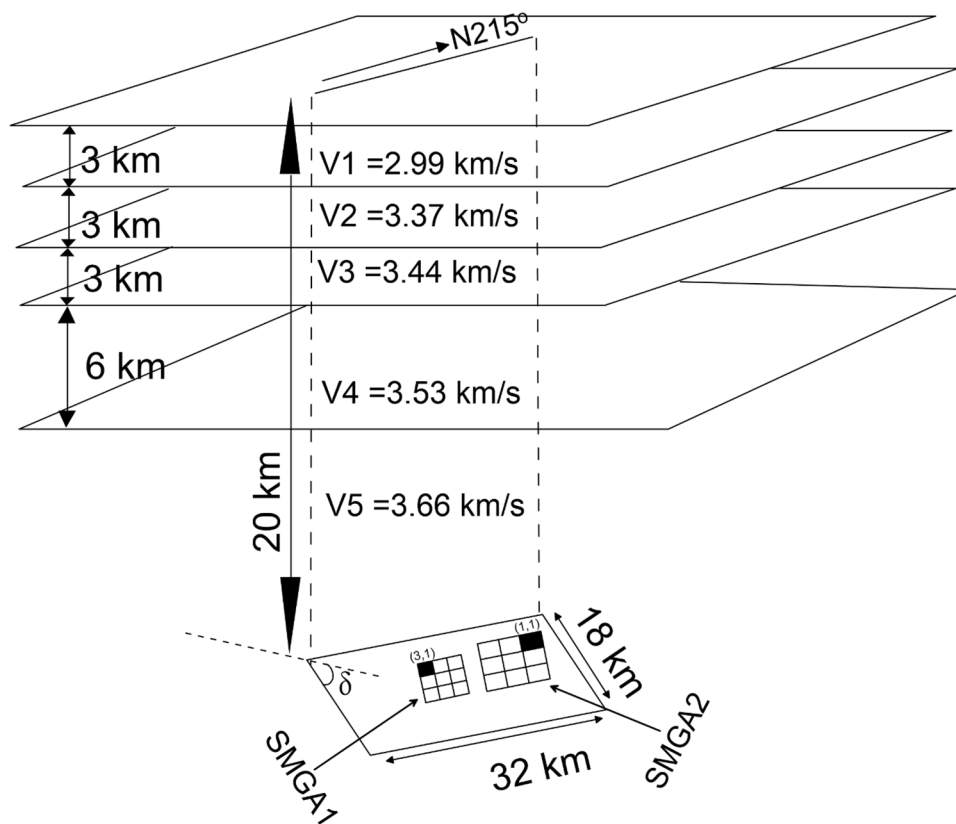


**Fig. 8** Source model with strike direction N215° and dip ( $\delta$ ) 46° is placed in the fifth layer of the velocity-layered media (Wen et al. 2019)

**Table 5** Modeling parameters of SMGAs for the final simulation

Modeling Parameters	SMGA1	SMGA2	Source
Length (km)	7.6	5.8	Wells and Coopersmith (1994)
Width (km)	5.3	4.4	Wells and Coopersmith (1994)
No. of sub-faults (N×N)	3×3	3×3	Scaling relation (Kanamori and Anderson 1975)
Strike	215	215	USGS
Dip	46	46	USGS
Rake	70	70	USGS
Vs (km/s)	3.5	3.5	Average velocity of the velocity model
Vr (km/s)	2.8	2.8	Mendoza and Hartzell (1988) and Reiter (1990)

## Scaling laws

The MSET is based on the empirical relation of the duration parameter ' $T_d$ ', and it also uses the frequency-dependent secondary wave quality factor ' $Q_\beta(f)$ ' of the region. The use of quality factor is to shape the propagation filter used in obtaining spectra having properties of earthquake acceleration spectra. The hypocenter of this earthquake is 20 km, as evaluated by United States Geological Survey (USGS). Therefore, the hypocenter of this earthquake lies within a zone of 30–35 km depth earthquakes defined by Sokolov et al. (2009).

The Moho depth for this region is 32–35 km (Li et al. 2014). The frequency-dependent quality factor defined by Sokolov et al. (2009) using earthquakes within the depth of 30–35 km is  $80 \times f^{0.9}$  and the same has been used in the present study. This relation has already been used to simulate the 2013 Nantou, Taiwan earthquake by Joshi et al. (2015). The shape of the envelope function used in SET depends on the duration parameter ' $T_d$ '. It is defined as the difference between the time of arrival of the peak and the onset time in the envelope of the accelerogram. This parameter is computed by utilizing the generalized regression relation

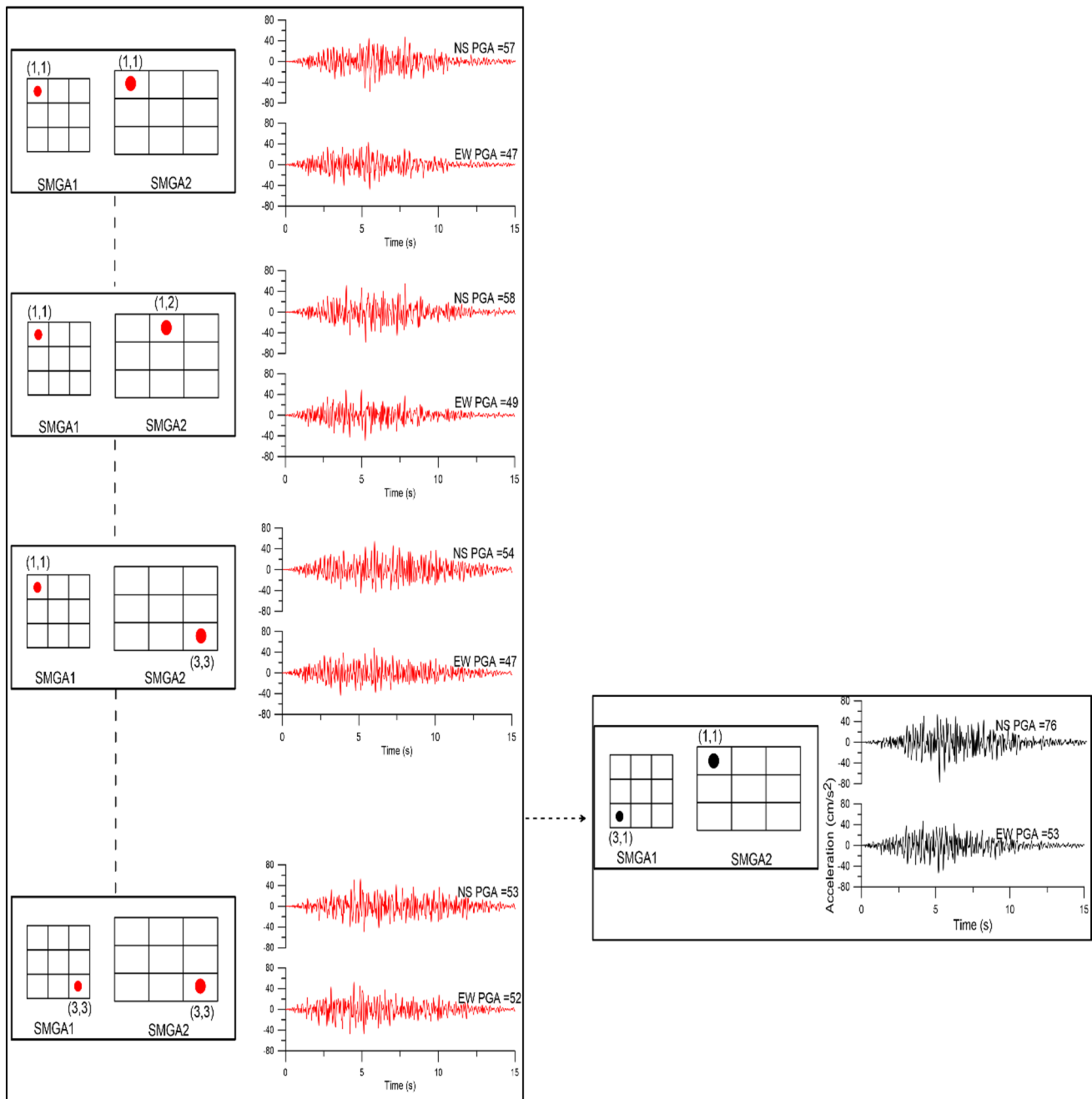


**Fig. 9** The procedure of selecting the optimal nucleation point among 81 possibilities of nucleation points. Simulated (red) horizontal components at TWD station for 81 nucleation points. The black record

shows minimum  $RMSE_{PGA}$  between synthetic and processed waveforms at the rock site

suggested by Midorikawa (1989) and further used by various workers Joshi and Midorikawa (2004), Joshi and Mohan (2010), Joshi et al. (2012a), Sandeep et al. (2014a, b, and 2019). In general form, this relation as suggested is given as:

$$T_d = 0.0015 \times 10^{0.5M_w} + a \times R^b, \quad (1)$$

where the distance of the station from the hypocenter is represented by  $R$  in km and  $M_w$  represents the moment magnitude. The coefficients 'a' and 'b' in the above equation have been estimated using nine accelerograms of the Hualien earthquake. Figure 3 is used to calculate the ' $T_d$ ' parameter.

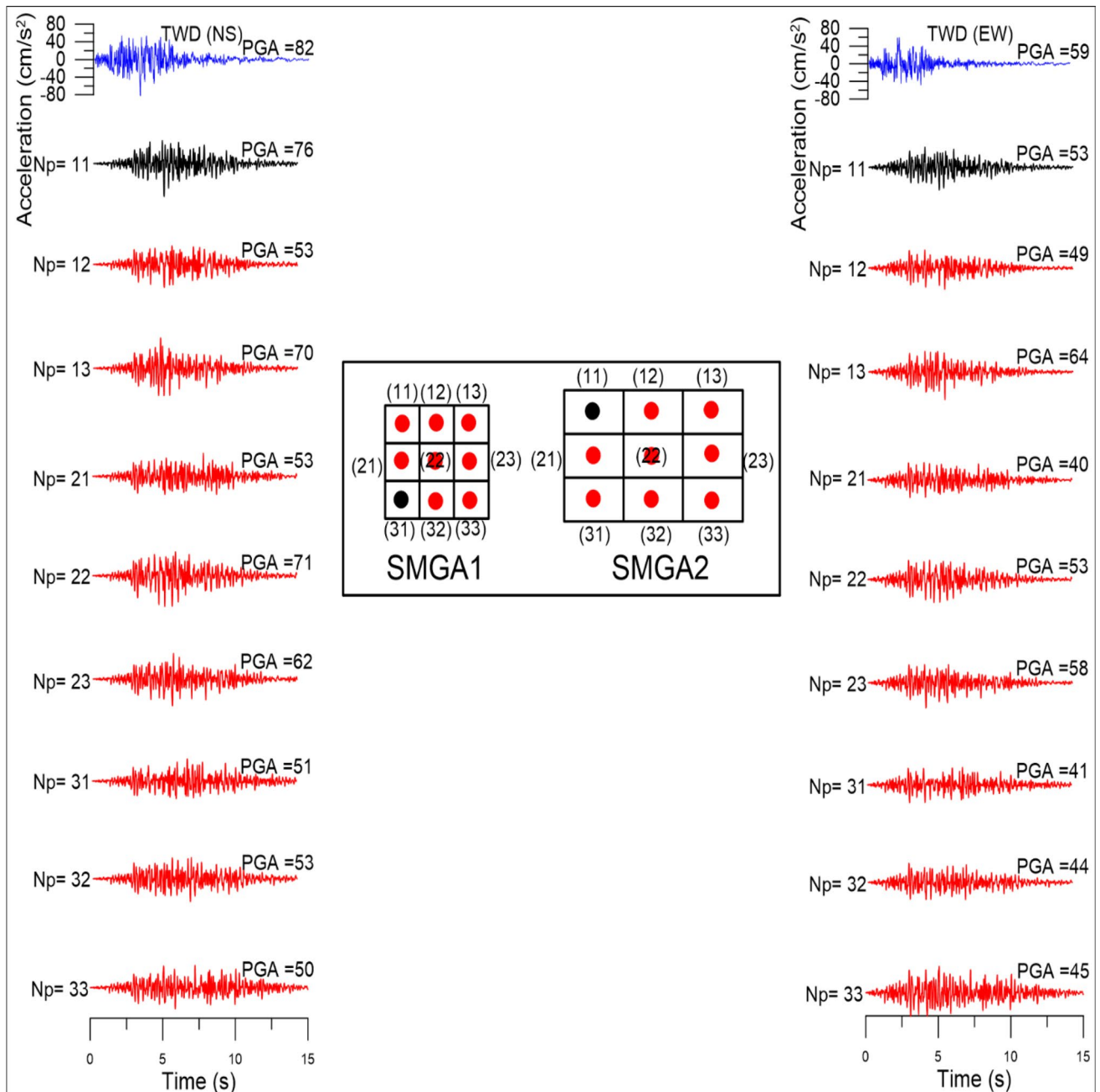


**Fig. 10** Simulated (red) horizontal components at TWD station to decide the nucleation point for both SMGA. Blue record is observed record at rock site. The black record shows minimum RMSE<sub>PGA</sub> between synthetic and processed waveforms at the rock site

The following regression relation for duration parameter 'T<sub>d</sub>' has been estimated from the data shown in Fig. 1 for modeling the Hualien earthquake:

$$T_d = 0.0015 \times 10^{0.5M_w} + 0.10 \times R^{0.85}. \tag{2}$$

### Strong motion generation area (SMGA) of the Hualien earthquake

The location of SMGAs is identified based on the spatiotemporal distribution of the aftershock of the 2019 Hualien earthquake reported by the strong motion network of the

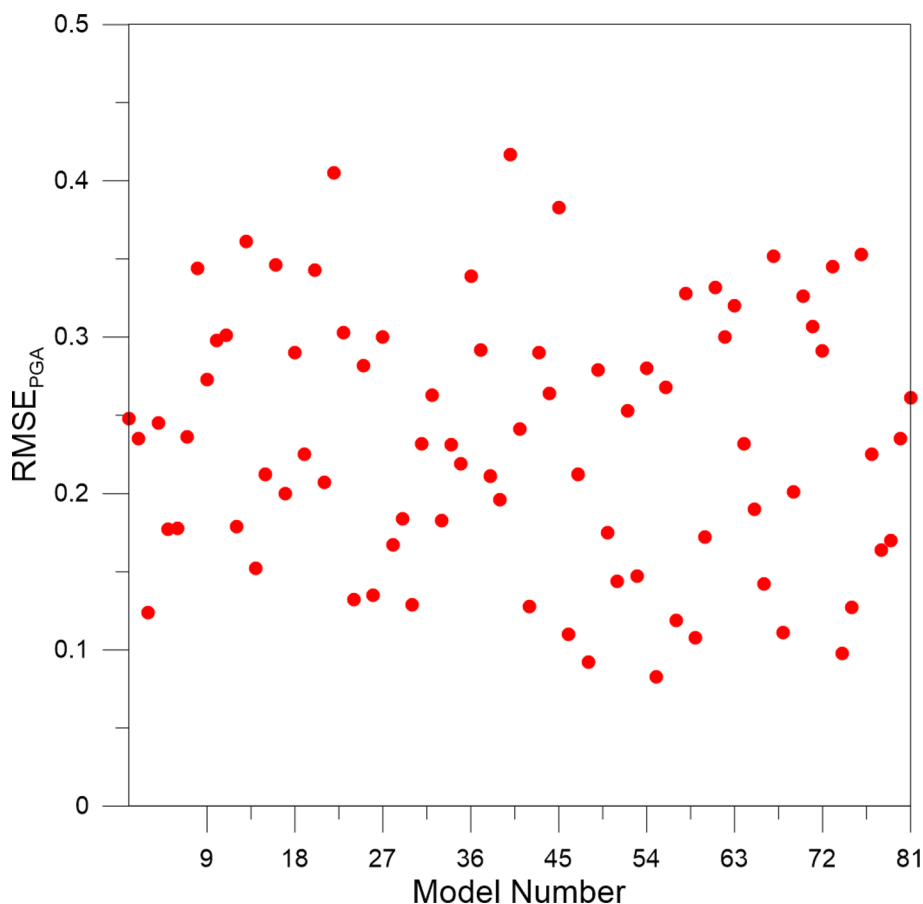


**Fig. 11**  $RMSE_{PGA}$  for various nucleation points

Central Weather Bureau (CWB) network between April 18, 2019, and May 3, 2019. A total of nineteen hundred six aftershocks were reported during the 15 days that are shown in Fig. 4. The source model of the mainshock indicating two SMGAs and the aftershocks distribution is shown in Fig. 4. The aftershocks are mostly distributed along the nodal plane1 (strike  $215^\circ$ , dip  $46^\circ$ ) of this earthquake. Therefore Lee et al. (2020) assumed a rupture plane of this earthquake dipping toward the west.

In MSET, SMGAs play a vital role. The source parameters of these two SMGAs play an equally important role in the simulation technique. In Fig. 5, the observed records at near-field stations from the epicenter are shown, indicating two SMGAs in the observed waveforms. Two wave packets can be seen visually at most of the recording stations, suggesting the possibility of two SMGAs. The aftershocks on the rupture plane also indicate the possibility of two SMGAs. SMGA1 is near to epicenter and the SMGA2 is located in the northern area of the epicenter. The seismic moment released when the rupture front passed through SMGA2 is large as compared to SMGA1. Lin et al. (2022) also reported two SMGAs for this earthquake using empirical Green's

function method. Lee et al. (2020) also studied the complex moment rate function of this earthquake and found that there is a larger burst of seismic energy releases from Asperity II than from Asperity I. The slip distribution studied by Lee et al. (2020) shows that slip of 50 cm and 100 cm has been observed on Asperity I and Asperity II, respectively.

The duration of envelopes of ground motion from these two SMGAs has been analyzed in the accelerogram at near-field stations in Fig. 5. This shows that the second phase represents a larger SMGA than the first phase. Figure 6a shows the location of stations used to study the time lags between identified SMGAs. The phases corresponding to identified SMGAs in the observed records at near-field stations are shown in Fig. 6b. Figure 6c shows the variation of time lags of two SMGAs with respect to the hypocentral distance of recording stations. The source displacement spectra (SDS) of the waveform representing two SMGAs at various stations have been used to evaluate the source parameters. The self-similarity laws given by Aki (1967), modified by Kanamori and Anderson (1975) have been used to divide SMGAs into sub-faults. This requires parameters of events representing



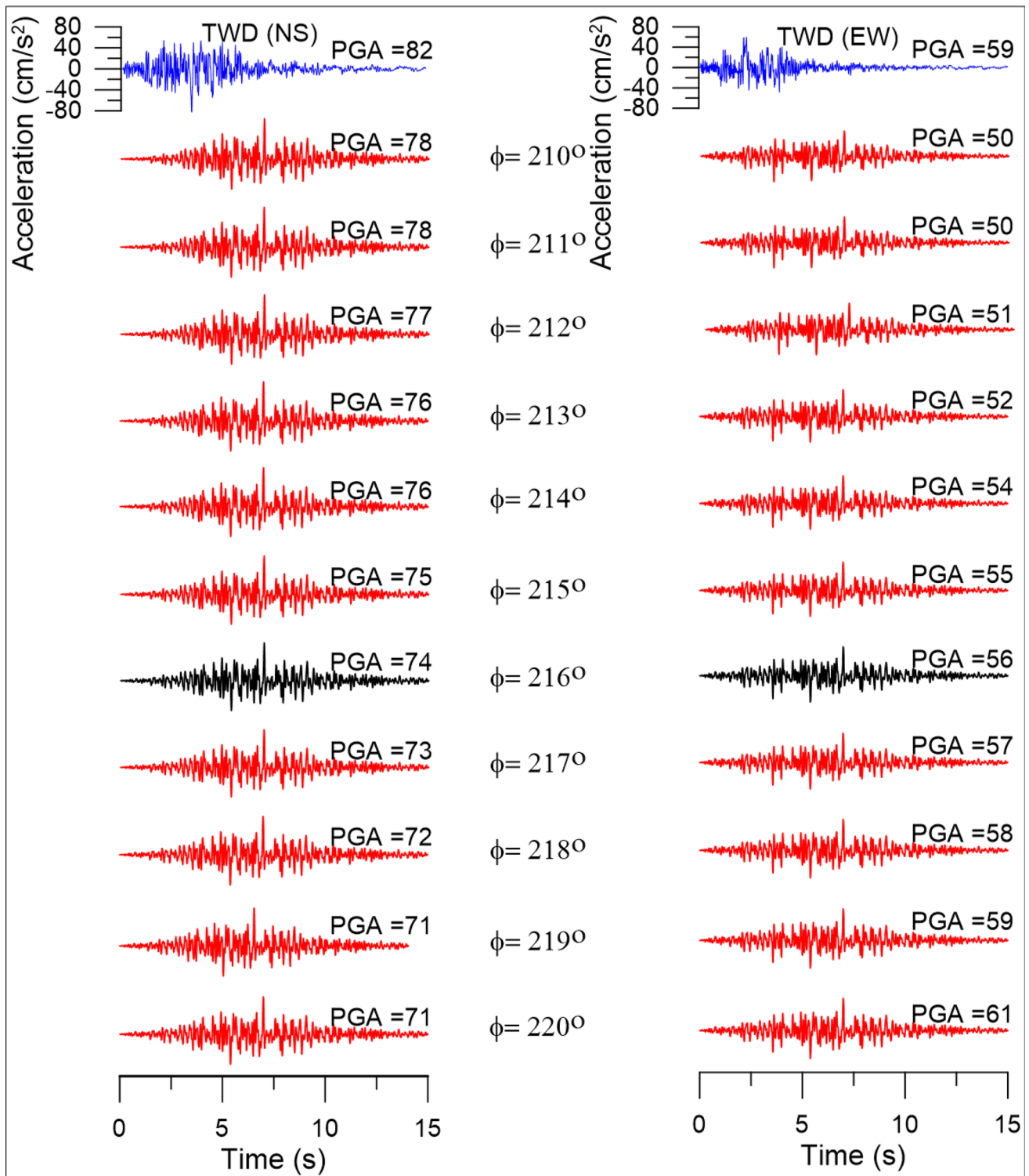


**Fig. 12** Simulated (red) horizontal components at the TWD station for different values of strike ( $\phi$ ) of the rupture plane. Blue record is observed record at rock site

sub-faults. The aftershock ( $M_L$  4.9) that occurred on May 23, 2019, has been used as a sub-event, and its location is shown in Fig. 6a. The source parameters of aftershock are

also calculated from SDS. The comparison of observed and theoretical SDS at TWD station for the N–S and E–W components of SMGA1, SMGA2, and the aftershock is depicted

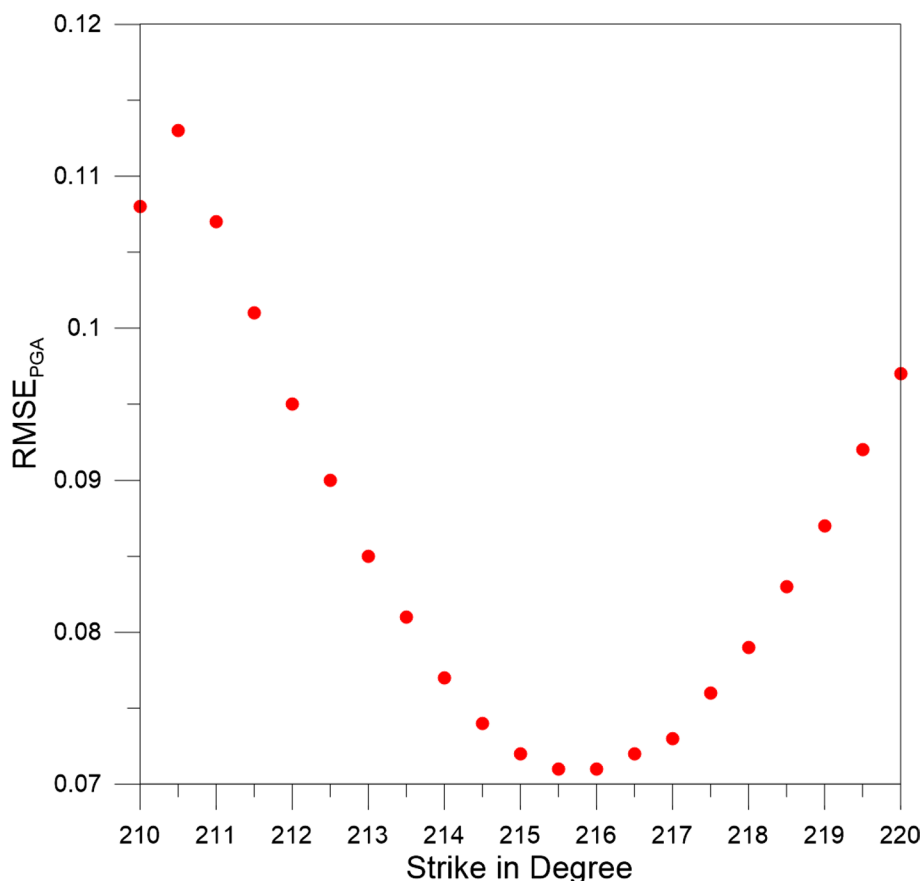


**Fig. 13** Plot of  $RMSE_{PGA}$  obtained from observed and simulated NS and EW components of accelerograms, respectively, at TWD station for various strike values

in Fig. 7. Source parameters of SMGA1, SMGA2, and after-shock evaluated from SDS are given in Table 4.

The downward extension and rupture length of the fault plane representing the Hualien earthquake have been calculated as 18 km and 32 km, respectively, using the relations proposed by Wells and Coppersmith (1994). The fault plane's dip and strike angle are kept at  $46^\circ$  and  $N215^\circ$ , respectively, at 20 km, as evaluated by United States Geological Survey (USGS). The rupture model was placed with strike direction  $N215^\circ$  and dip  $46^\circ$  in the last layer of the five-layer velocity model, as depicted in Fig. 8. Table 3 shows the  $V_s$  model used in this work, and it is given by Wen et al. (2019). The S wave velocity model given in Table 3 suggests an average S wave velocity of 3.5 km/s. As per the criteria given by Mendoza and Hartzell (1988) and Reiter (1990), the rupture velocity ( $V_r$ ) is considered to be 80% of shear wave velocity ( $V_s$ ). This gives an estimate of the rupture velocity as 2.8 km/s responsible for the rupture of the Hualien earthquake. Three reference rupture fronts with constant rupture velocities ( $V_r$ ) of 2 km/s, 3 km/s, and 4 km/s have been studied by Lee et al. (2020). We have tested these rupture velocities at a near-field station and concluded that

rupture fronts must have been moved with the speed of 3 km/s based on minimum  $RMSE_{PGA}$ .

Considering the rupture velocity of 2.8 km/s propagating along the length of 32 km rupture a ground motion of 11.4 s is calculated for the ideal condition. The significant duration of the SGM record at the TWD station is observed as 5.6 s. This indicates that the entire rupture of 32 km is not responsible for this earthquake, suggesting that two SMGAs can be present within the rupture plane. Visual inspection of SGM record at the TWD station indicates the possibilities of two main envelopes in the accelerogram, which indicate rupture propagation within two SMGAs responsible for producing SGM rather than within the entire rupture plane. The two SMGAs are named as SMGA1 and SMGA2 and are shown in Fig. 4. The dimensions of SMGA1 and SMGA2 are  $5.8 \times 4.4 \text{ km}^2$  and  $7.6 \times 5.3 \text{ km}^2$ , respectively, calculated using the relations proposed by Wells and Coppersmith (1994). The location of these SMGAs in the rupture responsible for this earthquake indicates that the depth of SMGA1 and SMGA2 is 27.5 km and 27.1 km, respectively, from the surface of the earth. In the MSET, the stress drop ( $\Delta\sigma$ ), corner frequency ( $f_0$ ), and seismic moment ( $M_0$ ) of events

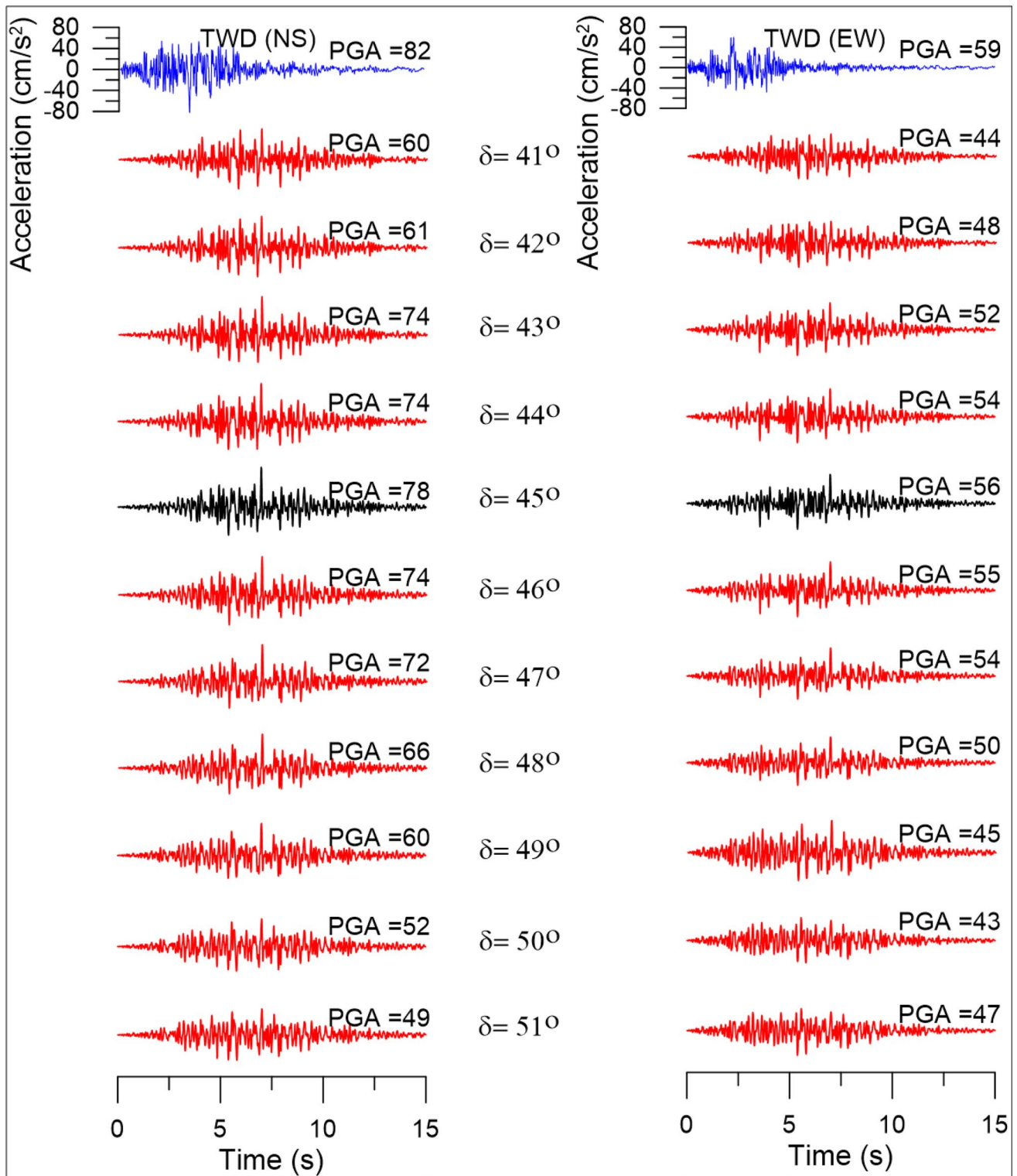


**Fig. 14** Simulated (red) horizontal components at the TWD station to decide the dip of the rupture plane. Blue record is observed record at rock site

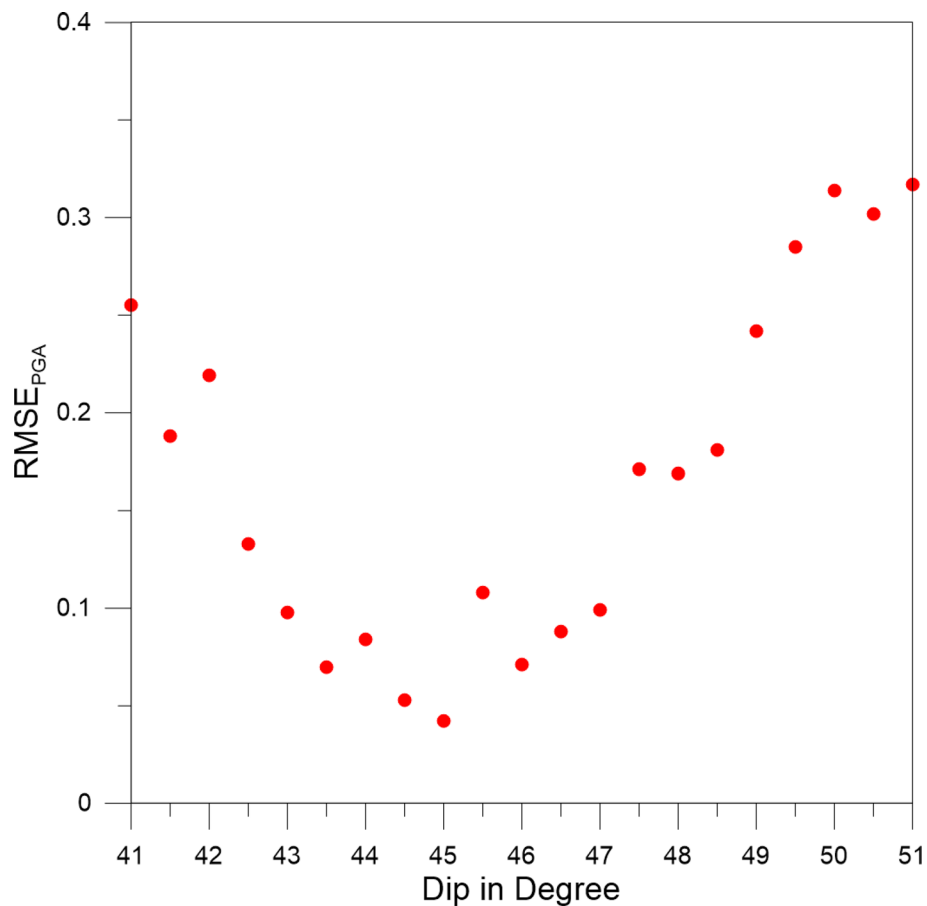


**Fig. 15** Plot of  $RMSE_{PGA}$  calculated from observed and simulated horizontal components of acceleration records, respectively, at TWD station for various dip values

referred to as SMGAs are required to model the plane of rupture to an earthquake that has been computed from SDS of these SMGAs given in Table 4. The patches responsible for SMGAs in the record have been used for obtaining SDS after proper corrections in the acceleration spectra. Main corrections that are needed include correction for geometrical spreading and anelastic attenuations. The SDS and the parameters are shown in Fig. 6 and Table 4, respectively.

## Results and discussions

### Selection of final rupture model

The SMGAs are divided into the number of sub-faults using the aftershock's seismic moment of the Hualien earthquake. The self-similarity laws suggest that both SMGA1 and SMGA2 can be divided into 9 sub-faults each representing  $3 \times 3$  sub-faults along the length and downward extension, respectively. Table 5 shows the final

modeling parameters of SMGAs of the rupture of the 2019 Hualien earthquake.

It is an important task to locate the nucleation point on the proposed SMGAs. Two SMGAs of size  $3 \times 3$  each give rise to the possibility of 81 nucleation points. All of these are the possibilities of nucleation points that have been tested, and the procedure of selecting nucleation points is explained in Fig. 9. In this process, the nucleation point in SMGA1 has been fixed, while all nine possibilities of nucleation point have been checked in SMGA2. The selection of the model is based on the following root-mean-square error (RMSE) between the PGA at NS and EW components at the selected station:

$$RMSE_{PGA} = \sqrt{\left(\frac{1}{2}\right) \cdot \left[ \left( \frac{PGA_{sim,NS} - PGA_{obs,NS}}{PGA_{obs,NS}} \right)^2 + \left( \frac{PGA_{sim,EW} - PGA_{obs,EW}}{PGA_{obs,EW}} \right)^2 \right]}, \quad (3)$$

where  $PGA_{sim,NS}$  and  $PGA_{sim,EW}$  are the PGA obtained from simulated N–S and E–W components and  $PGA_{obs,NS}$  and  $PGA_{obs,EW}$  are PGA values from observed N–S and

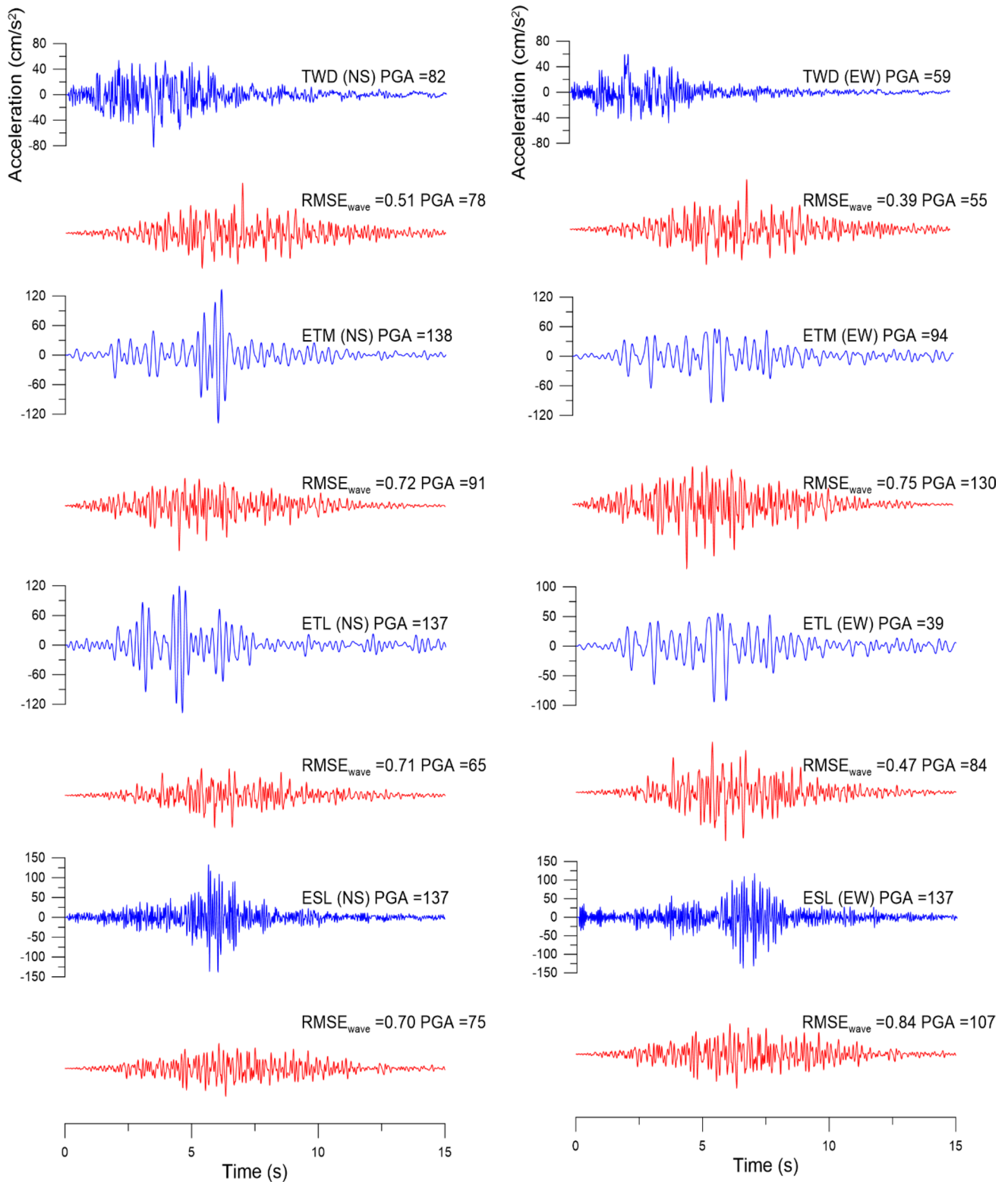


**Fig. 16** Comparison of N-S and E-W components obtained from simulated (red) and observed (blue) accelerograms at rock site at TWD, ETM, ETL, ESL stations



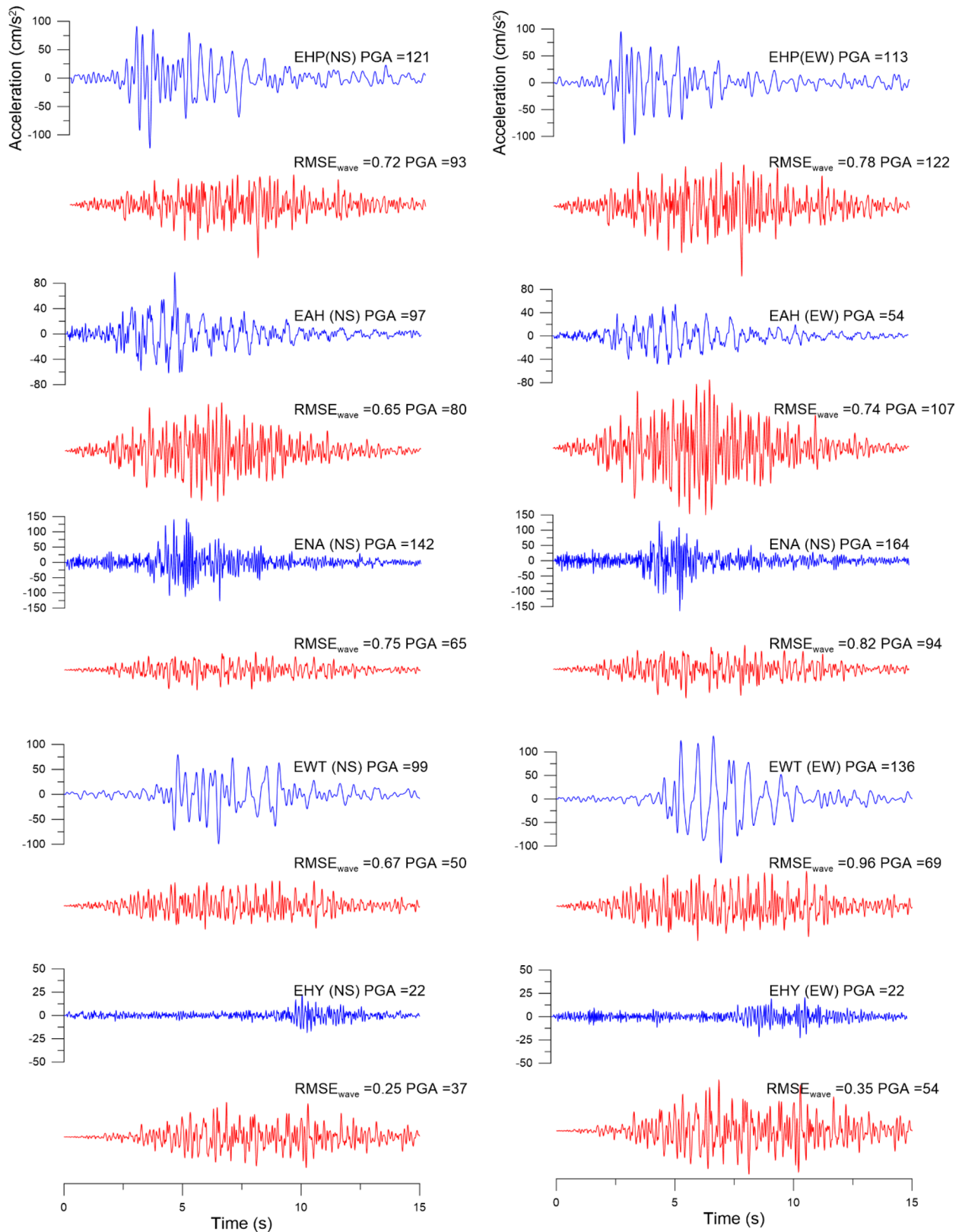


**Fig. 17** Comparison of N-S and E-W components obtained from simulated (red) and observed (blue) accelerograms at rock sites at EHP, EAH, ENA, EWT, and EHY stations

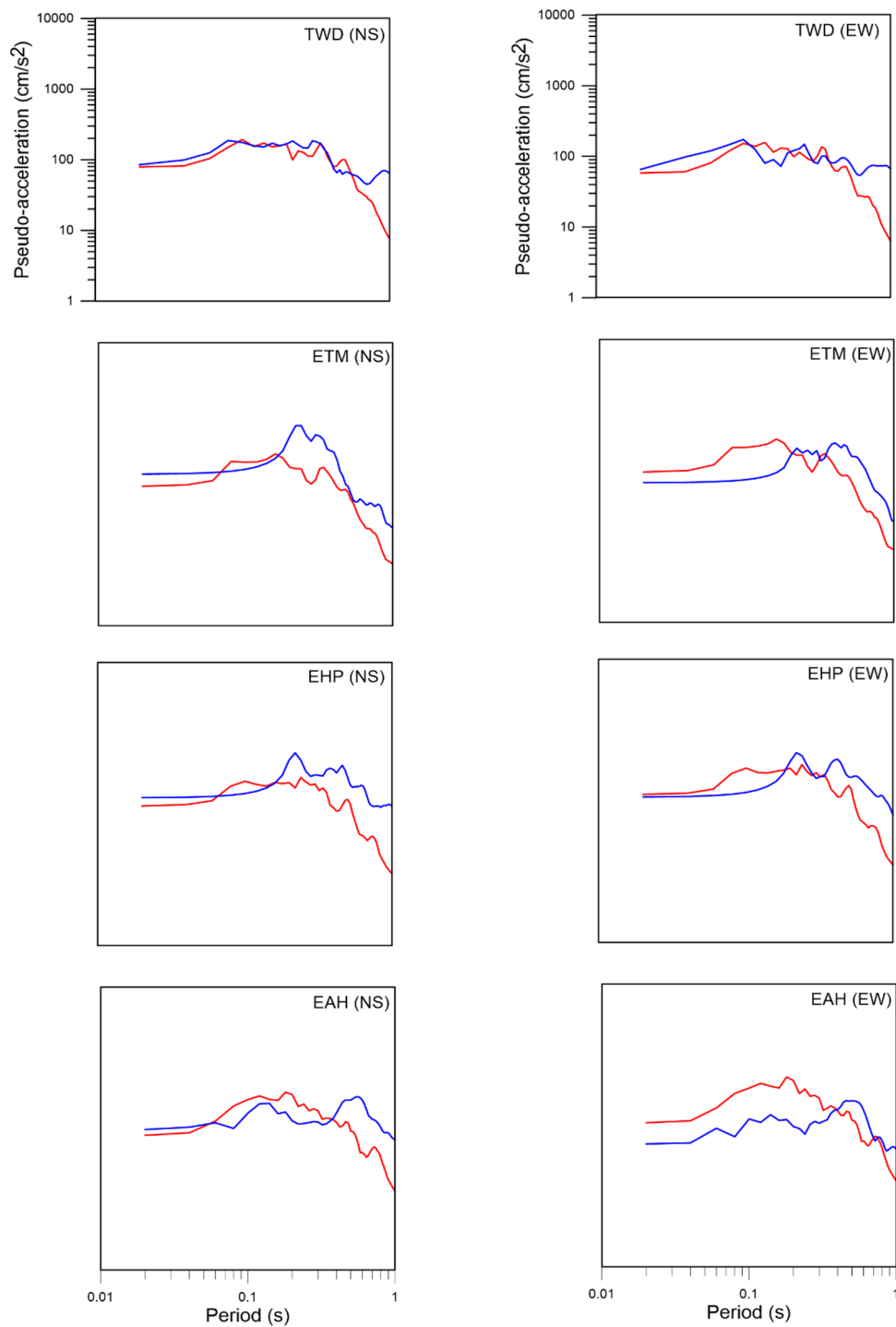


**Fig. 18** Comparison of response spectra of horizontal components obtained from observed (blue) and synthetic (red) accelerograms at rock sites at TWD, ETM, EHP, and EAH stations

E–W components of acceleration record. The simulated records and their comparison with the observed record for nine different possibilities of nucleation point in SMGA2 by fixing the position of nucleation point in SMGA1 are shown

in Fig. 10. Figure 11 represents the  $RMSE_{PGA}$  for different possibilities of nucleation points and obtained PGA from both horizontal components. The maximum PGA obtained from various models varies from 38 to 76  $cm/s^2$  in both

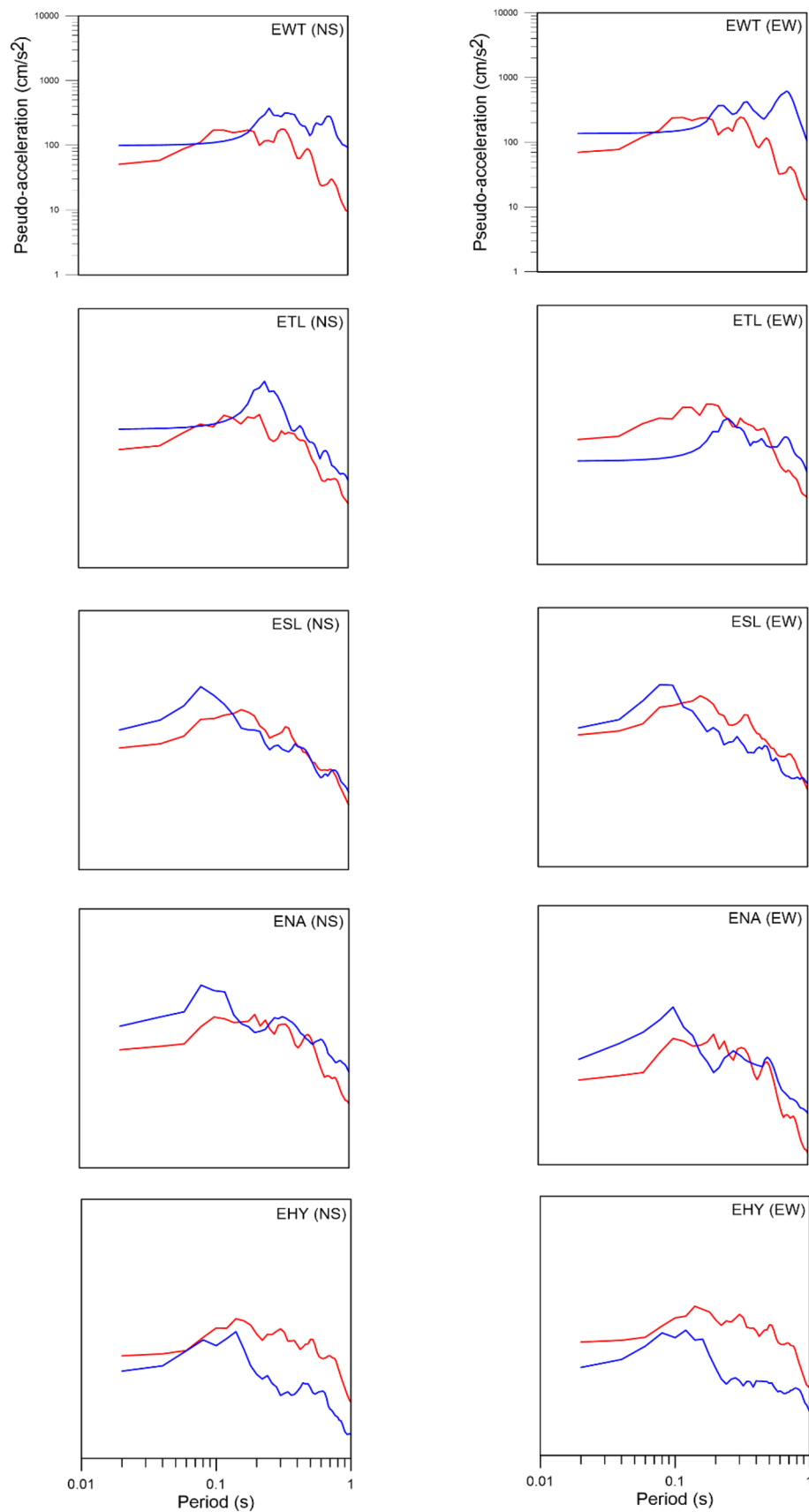


**Fig. 19** Comparison of response spectra of horizontal components obtained from observed (blue) and synthetic (red) accelerograms at rock sites at EWT, ETL, ESL, ENA, and EHY stations

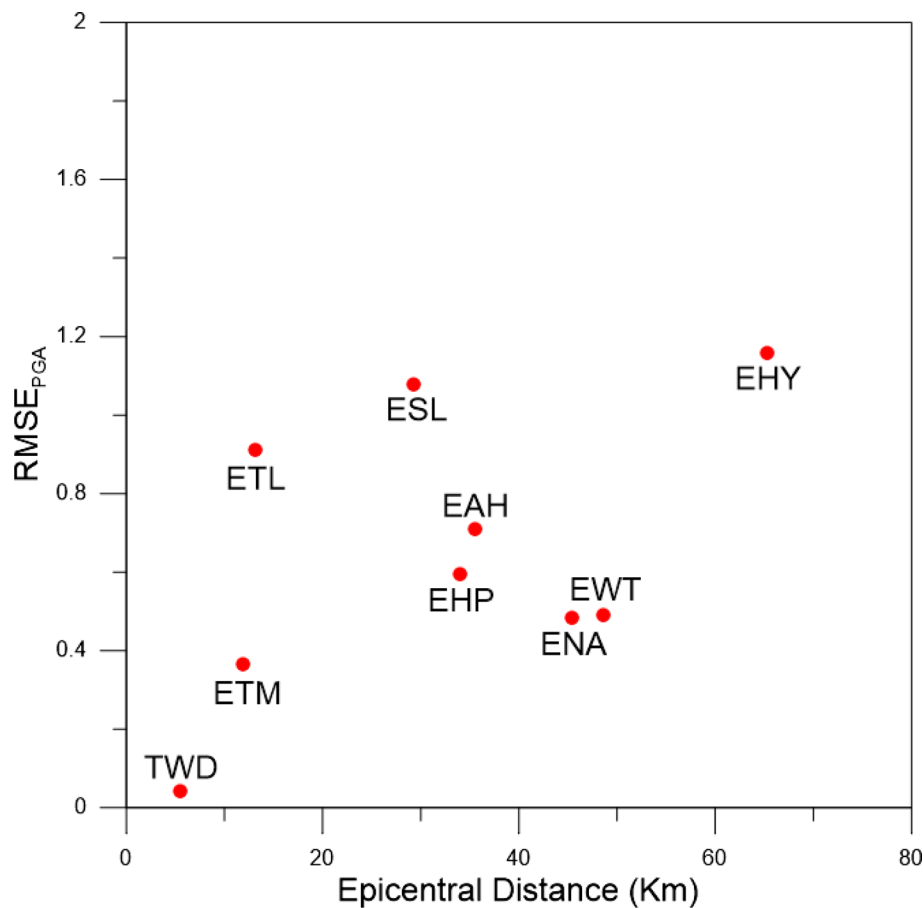


**Fig. 20** Plot of  $RMSE_{PGA}$  at various stations obtained from comparison of PGA value from synthetic and observed accelerograms due to final rupture model

components. For this selection, the range of  $RMSE_{PGA}$  is from 0.08 to 0.41, which is very high suggesting the important role of the nucleation point in the modeling parameters. It is seen that minimum  $RMSE_{PGA}$  has been obtained for models having nucleation points at extreme left corners and the same has been retained for further modeling.

Once the nucleation point has been fixed, the rupture plane's strike has been changed iteratively in a range between  $N210^{\circ}$ – $N220^{\circ}$  with an interval of  $0.5^{\circ}$  and fixing the other modeling parameters as given in Table 5. For each strike value, the acceleration record has been simulated at the TWD station. The maximum PGA obtained from various strike varies from 49 to  $78 \text{ cm/s}^2$  in both components. Figure 12 shows the simulated acceleration records for various values of strike selection for the rupture model. The plot of  $RMSE_{PGA}$  for different possible models in Fig. 13 shows that it is minimum for strike direction of  $N215.5^{\circ}$  based on the

minimum  $RMSE_{PGA}$  between the PGA obtained from synthetic and observed acceleration records at the TWD station.

We finalized the dip amount by selecting the model that gives minimum  $RMSE_{PGA}$  among models assumed by varying dip between  $41^{\circ}$  and  $51^{\circ}$  with an interval of  $0.5^{\circ}$  and fixing the other modeling parameters as given in Table 5. For each dip value, the acceleration record has been simulated at the TWD station. The maximum PGA obtained from various dip varies from 42 to  $78 \text{ cm/s}^2$  in both components. Figure 14 shows the simulated records at the TWD station obtained by different models that differ by dip amount. The  $RMSE_{PGA}$  for various models that differ by dip amount is shown in Fig. 15. Among these, the model having dip  $45^{\circ}$  gives minimum  $RMSE_{PGA}$  and has been retained for further simulation.

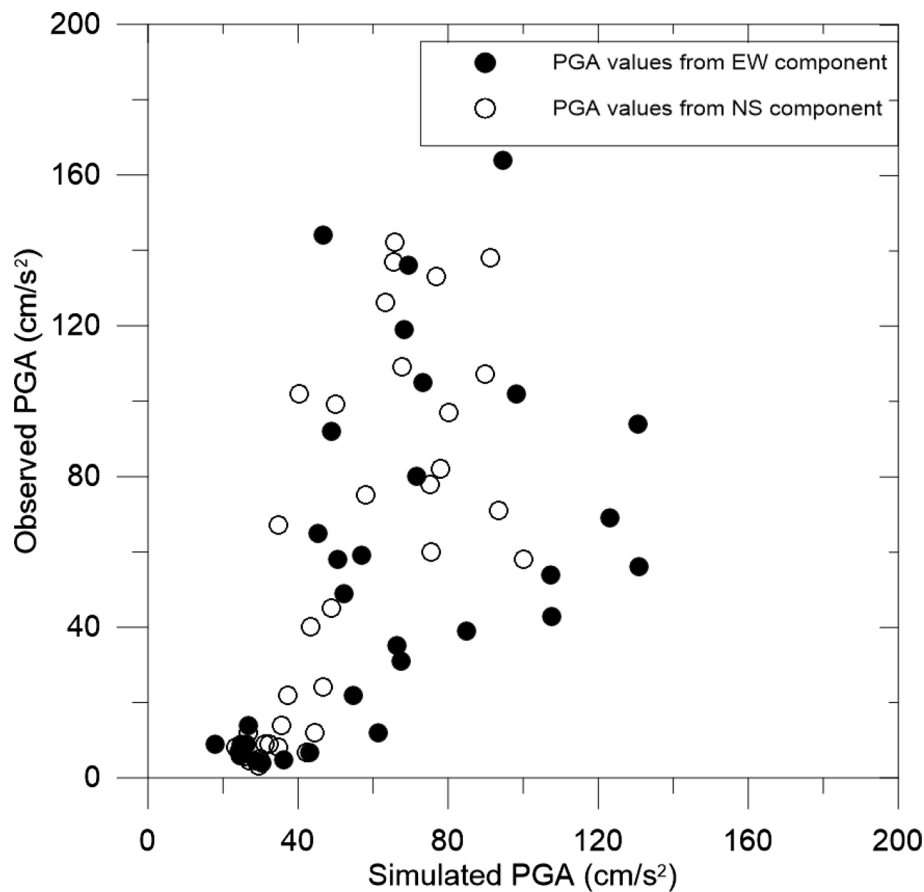


Fig. 21 Comparison of PGA obtained from observed and simulated horizontal components at various stations

### Strong motion simulation of 2019 Hualien earthquake

Once all the parameters have been finalized, the rupture model has been utilized to simulate SGM records at thirty-three stations that have recorded this earthquake that lies at an epicentral distance ranging from 5 to 100 km. The simulated records are compared based on waveform comparison,  $RMSE_{wave}$  by using the following formula:

$$RMSE_{wave} = \left[ \left( \sum_{n=1}^{n=N} (A^{sim}(n) - A^{obs}(n))^2 \right)^{\frac{1}{2}} \right] \cdot \left( \frac{1}{N} \right). \quad (4)$$

In this formula,  $A^{sim}(n)$  and  $A^{obs}(n)$  are the simulated and observed records containing  $N$  number of samples. The comparison of synthetic and observed records obtained from the final model at nine stations is shown in Figs. 16, 17. The response spectra obtained from observed and synthetic records for these nine stations are shown in Figs. 18, 19. The  $RMSE_{PGA}$  from observed and synthetic records has been computed at these stations, which are shown in Fig. 20. One

of the striking features of this earthquake is that although TWD station is at a distance of 6 km from the epicenter, this station recorded a low PGA of  $59 \text{ cm/s}^2$  in the horizontal component (Table 2). The same trend is also visible in the simulated records shown in Fig. 16. Minimum  $RMSE_{wave}$  and  $RMSE_{PGA}$  have been observed at EHY station and TWD station, respectively.

The PGA obtained from simulated accelerograms has been compared with that obtained from observed accelerograms at stations lying within the epicentral distance of 100 km, and it is shown in Fig. 21. The comparison shows the final selected model simulated records that compare PGA values at various stations in horizontal components. The distribution of PGA computed from observed and simulated records and calculated using the attenuation relation given by (Lin and Lee 2008) with respect to epicentral distance is shown in Fig. 22. Comparison of PGA in Figs. 21 and 22 shows that the finally selected model with two SMGAs can simulate records with realistic shape and reliable statistical properties. Figure 23 shows the contours plotted for observed and simulated NS and EW components,



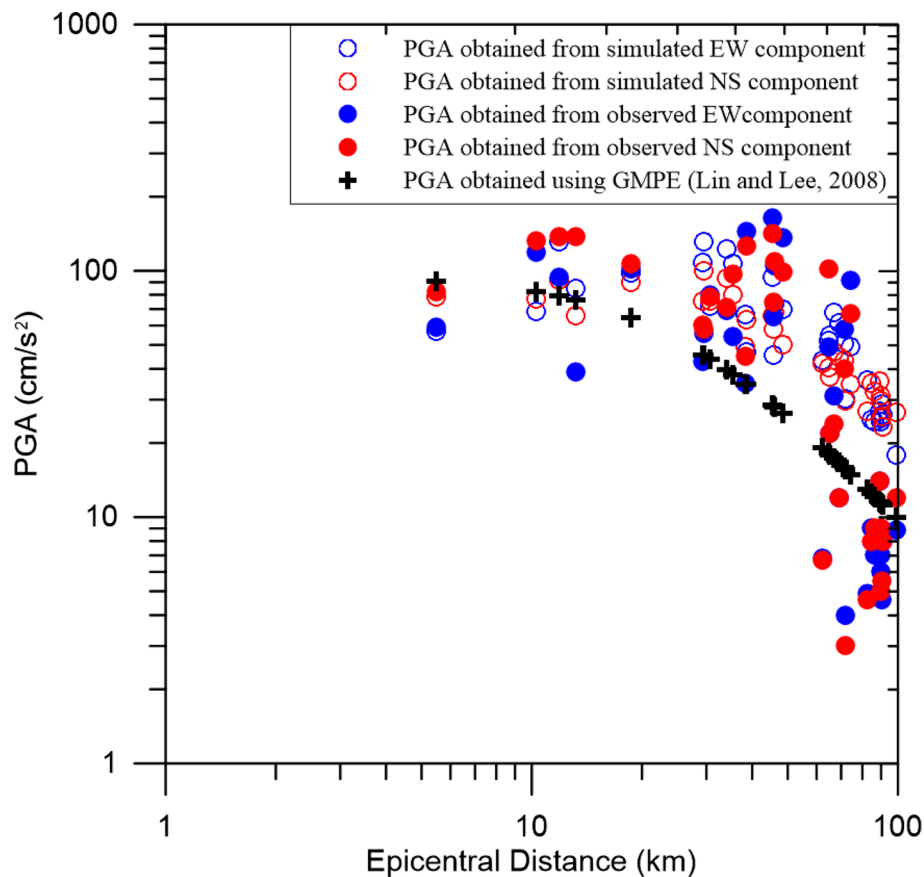


**Fig. 22** Distribution of PGA computed from observed and simulated records and calculated using attenuation relation given by Lin and Lee (2008) with respect to epicentral distance

respectively, for each station. The trend of the contours shows northward rupture of this earthquake caused a strong directivity effect, which follows the study done by Lee et al. (2020). The difference in the isoacceleration contours have been attributed to the consideration of simple velocity model consisting of layered earth system which possibly deviates from actual earth scenario.

## Conclusions

The rupture responsible for the Hualien earthquake of magnitude ( $M_w$  6.1) has been modeled in this paper. Two SMGAs named SMGA1 and SMGA2 have been identified within the rupture plane for this earthquake based on aftershock distribution and the shape of accelerograms at various stations. The source parameters of the SMGAs have been calculated from the source spectrum and have been further utilized to model

the rupture consisting of these two SMGAs. Iterative modeling of rupture parameters like dip, strike, and location of nucleation point has been performed to select the final rupture model. RMSE in terms of PGA obtained from both E–W and N–S components of observed and synthetic record at TWD station has been used to finalize rupture's parameter of this earthquake. The finalized rupture parameters have been further utilized to simulate SGM at several other stations that lie at a distance of 5–100 km from the epicenter.

The observed and simulated waveforms and their respective pseudo-acceleration response spectra have been compared. The comparison of PGA with the attenuation relation given by Lin and Lee (2008) clearly shows that the model is effectively predicting PGA with reasonable accuracy within 100 km epicentral distance. The comparison of observed and simulated records at various stations indicates that the rupture of this earthquake is characterized by two SMGAs.

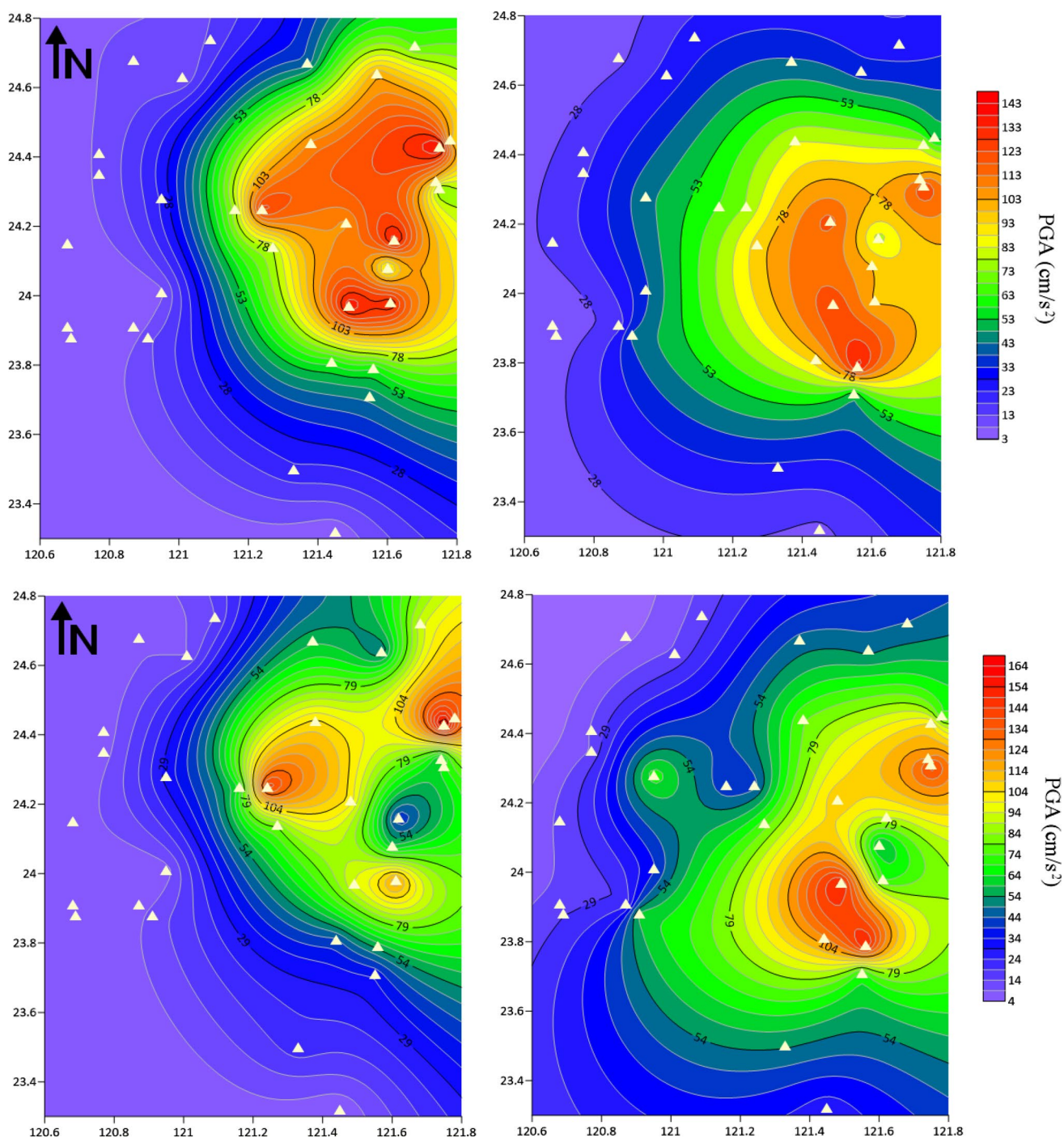


**Fig. 23** Contours of PGA ( $\text{cm/s}^2$ ) computed from: (a) observed NS component, (b) simulated NS component, (c) observed EW component, and (d) simulated EW component. Stations are represented by solid triangles

**Acknowledgements** The acceleration waveform data and aftershocks data of the April 18, 2019, Hualien earthquake are provided by Geophysical Database Management System (GDMS). This is a web-based data service platform in Taiwan that is constructed by Central Weather Bureau (CWB). The data provided by CWB for this work are highly acknowledged. The authors would like to offer special thanks to Indian Institute of Technology Roorkee for the support required for

the research work shown in this paper. Project grant No. GITA/DST/TWN/P-75/2017 approved by Department of Science and Technology (DST), Government of India, has been highly acknowledged.

**Author Contributions** Saurabh Sharma has done the formal analysis and research work presented in this paper using MSET. A. Joshi supervised the whole research work methodology. Sandeep has helped with

his experience in the simulation technique used in this paper. C.-M. Lin, C.-H. Kuo, and K.-L. Wen have provided the data and also their valuable comments regarding the work presented. S. Singh and M.L. Sharma have helped in the planning and execution of the manuscript. Mohit Pandey and Jyoti Singh have helped in writing the initial draft and data presentation. All the named authors provided their critical feedback on data interpretation and supported the improvement of the manuscript.

**Funding** This research work is done under project Grant No. GITA/DST/TWN/P-75/2017 approved by Department of Science and Technology, Government of India.

**Availability of data and material** The data used in this research work are provided by Central Weather Bureau (CWB).

**Code availability** Self-developed code in FORTRAN.

## Declarations

**Conflict of interest** We declare that there are no competing interests related to any financial concern about the publication of a study.

**Human and animal rights** It is being declared that there are no personal relationships with people or organizations that may influence or may be perceived to influence the research work described in this paper.

## References

- Aki K (1967) Scaling law of seismic spectrum. *J Geophys Res* 72(4):1217–1231
- Aki K, Richards PG (2002) University Science Books. Sausalito, California.
- Atkinson GM, Boore DM (1995) Ground-motion relations for eastern North America. *Bull Seismol Soc Am* 85(1):17–30
- Boore DM (1983) Stochastic simulation of high-frequency ground motions based on seismological models of the radiated spectra. *Bull Seismol Soc Am* 73(6A):1865–1894
- Brune JN (1970) Tectonic stress and the spectra of seismic shear waves from earthquakes. *J Geophys Res* 75(26):4997–5009
- Chin SJ, Lin JY, Chen YF, Wu WN, Liang CW (2016) Transition of the Taiwan-Ryukyu collision-subduction process as revealed by ocean-bottom seismometer observations. *J Asian Earth Sci* 128:149–157
- Erdik M, Durukal E (2004) Strong ground motion. In: *Recent advances in earthquake geotechnical engineering and microzonation* (pp. 67–100). Springer, Dordrecht.
- Frankel A (1991) High-frequency spectral falloff of earthquakes, fractal dimension of complex rupture, b value, and the scaling of strength on faults. *J Geophys Res: Solid Earth* 96(B4):6291–6302
- Hanks TC, McGuire RK (1981) The character of high-frequency strong ground motion. *Bull Seismol Soc Am* 71(6):2071–2095
- Hartzell SH (1978) Earthquake aftershocks as Green's functions. *Geophys Res Lett* 5(1):1–4
- Idriss IM, Sun JI (1992) SHAKE91: A computer program for conducting equivalent linear seismic response analyses of horizontally layered soil deposits. Center for Geotechnical Modeling, Department of Civil and Environmental Engineering, University of California, Davis, CA
- Irikura K (1983) Semi-empirical estimation of strong ground motions during large earthquakes. *Bull Dis Prevent Res Institute* 33(2):63–104
- Irikura K (1986) Prediction of strong acceleration motion using empirical Green's function. In: *Proc. 7th Japan Earthq. Eng. Symp* (Vol. 151, pp. 151–156).
- Irikura K, Kagawa T, Sekiguchi H (1997) Revision of the empirical Green's function method. In: *Program and abstracts of the seismological society of Japan* (Vol. 2, No. B25).
- Irikura K, Kamae K (1994) Estimation of strong ground motion in broad-frequency band based on a seismic source scaling model and an empirical Green's function technique.
- Joshi A (1997) Modelling of peak ground accelerations for Uttarkashi Earthquake of 20th October, 1991. *Bull Indian Soc Earthquake Technol* 34(2):75–96
- Joshi A, Patel RC (1997) Modelling of active lineaments for predicting a possible earthquake scenario around Dehradun, Garhwal Himalaya. *India Tectonophys* 283(1–4):289–310
- Joshi A, Kumar B, Sinvhal A, Sinvhal H (1999) Generation of synthetic accelerograms by modelling of rupture plane. *ISET J Earthq Technol* 36(1):43–60
- Joshi A (2001) Strong motion envelope modelling of the source of the Chamoli earthquake of March 28, 1999 in the Garhwal Himalaya. *India J Seismol* 5(4):499–518
- Joshi A, Singh S, Giroti K (2001) The simulation of ground motions using envelope summations. *Pure Appl Geophys* 158(5):877–901
- Joshi A (2004) A simplified technique for simulating wide-band strong ground motion for two recent Himalayan earthquakes. *Pure Appl Geophys* 161(8):1777–1805
- Joshi A, Midorikawa S (2004) A simplified method for simulation of strong ground motion using finite rupture model of the earthquake source. *J Seismolog* 8(4):467–484
- Joshi A, Mohan K (2010) Expected peak ground acceleration in Uttarakhand Himalaya, India region from a deterministic hazard model. *Nat Hazards* 52(2):299–317
- Joshi A, Kumari P, Sharma ML, Ghosh AK, Agarwal MK, Ravikiran A (2012a) A strong motion model of the 2004 great Sumatra earthquake: simulation using a modified semi empirical method. *J Earthquake and Tsunami* 6(04):1250023
- Joshi A, Kumari P, Singh S, Sharma ML (2012b) Near-field and far-field simulation of accelerograms of Sikkim earthquake of September 18, 2011 using modified semi-empirical approach. *Nat Hazards* 64(2):1029–1054
- Joshi A, Sandeep K (2014) Modeling of strong motion generation areas of the 2011 Tohoku, Japan earthquake using modified semi empirical technique. *Nat Hazards* 71:587–609
- Joshi A, Kuo CH, Dhibar P, Sharma ML, Wen KL, Lin CM (2015) Simulation of the records of the 27 March 2013 Nantou Taiwan earthquake using modified semi-empirical approach. *Nat Hazards* 78(2):995–1020
- Joyner WB, Boore DM (1986) On simulating large earthquakes by Green's function addition of smaller earthquakes. *Earthquake Source Mech* 37:269–274
- Kanai K (1951) Relation between the nature of surface layer and the amplitude of earthquake motions. *Bull Earthquake Res Institute*.
- Kanamori H (1979) A semi-empirical approach to prediction of long-period ground motions from great earthquakes. *Bull Seismol Soc Am* 69(6):1645–1670
- Kanamori H, Anderson DL (1975) Theoretical basis of some empirical relations in seismology. *Bull Seismol Soc Am* 65(5):1073–1095
- Kumar D, Khattri KN (2002) A study of observed peak ground accelerations and prediction of accelerograms of 1999 Chamoli earthquake. *Himalayan Geol* 23(1):51–61
- Kumar D, Khattri KN, Teotia SS, Rai SS (1999) Modelling of accelerograms of two Himalayan earthquakes using a novel semi-empirical method and estimation of accelerogram for a hypothetical great earthquake in the Himalaya. *Current Science*, pp. 819–830.

- Kuo-chen H, Vu YM, Chang CH, Hu JC, Chen WS (2004) Relocation of eastern Taiwan earthquakes and tectonic implications. *Terrestrial Atmospheric and Oceanic Sci* 15:647–666
- Lal S, Joshi A, Tomer M, Kumar P, Kuo CH, Lin CM, Sharma ML (2018) Modeling of the strong ground motion of 25th April 2015 Nepal earthquake using modified semi-empirical technique. *Acta Geophys* 66(4):461–477
- Lee SJ, Wong TP, Liu TY, Lin TC, Chen CT (2020) Strong ground motion over a large area in northern Taiwan caused by the northward rupture directivity of the 2019 Hualien earthquake. *J Asian Earth Sci* 192:104095
- Li Z, Roecker S, Kim K, Xu Y, Hao T (2014) Moho depth variations in the Taiwan orogen from joint inversion of seismic arrival time and Bouguer gravity data. *Tectonophysics* 632:151–159
- Lin PS, Lee CT (2008) Ground-motion attenuation relationships for subduction-zone earthquakes in northeastern Taiwan. *Bull Seismol Soc Am* 98(1):220–240
- Lin Y, Yi-Ying W, Yin-Tung Y (2022). Source properties of the 2019 ML6. 3 Hualien, Taiwan, earthquake, determined by the local strong motion networks. *Geophysical J Int*.
- Lysmer J, Bolton SH, Schnabel PB (1971) Influence of base-rock characteristics on ground response. *Bull Seismol Soc Am* 61(5):1213–1231
- Mendoza C, Hartzell SH (1988) Inversion for slip distribution using teleseismic P waveforms: North Palm Springs, Borah Peak, and Michoacán earthquakes. *Bull Seismol Soc Am* 78(3):1092–1111
- Midorikawa S (1989) Synthesis of ground acceleration of large earthquakes using acceleration envelope waveform of small earthquake. *J Struct Construct Eng* 398:23–30
- Midorikawa S (1993) Semi-empirical estimation of peak ground acceleration from large earthquakes. *Tectonophysics* 218(1–3):287–295
- Mittal H, Benjamin MY, Tai-Lin T, Yih-Min W (2021) Importance of real-time PGV in terms of lead-time and shakemaps: results using 2018 ML 6. 2 & 2019 ML 6. 3 Hualien Taiwan earthquakes. *J Asian Earth Sci* 220:1049
- Miyake H, Iwata T, Irikura K (2003) Source characterization for broadband ground-motion simulation: Kinematic heterogeneous source model and strong motion generation area. *Bull Seismol Soc Am* 93(6):2531–2545
- Miyahara M, Sasatani T (2004) Estimation of source process of the 1994 Sanriku Haruka-oki earthquake using empirical Green's function method. *Geophys Bull Hokkaido Univ Sapporo Japan* 67:197–212 (in Japanese with English abstract)
- Reiter L (1990) Earthquake hazard analysis: issues and insights (Vol. 22, No. 3, p. 254). New York: Columbia University Press.
- Sandeep, Joshi A, Kamal, Kumar P, Kumar A (2014a) Effect of frequency dependent radiation pattern in simulation of high frequency ground motion of Tohoku earthquake using modified semi empirical method. *Nat Hazards*, 73: 1499-1521
- Sandeep, Joshi A, Kamal, Kumar P, Kumari P (2014b) Modeling of strong motion generation area of the Uttarkashi earthquake using modified semi-empirical approach. *Nat. Hazards*, 73: 2041–2066
- Sandeep, Joshi A, Sah SK, Kumar P, Lal S, Kamal (2019) Modeling of strong motion generation areas for a great earthquake in central seismic gap region of Himalayas using the modified semi-empirical approach. *J Earth Syst Sci*
- Schnabel PB, Lysmer J, Seed HB (1972) SHAKE: a computer program for earthquake response analysis of horizontally layered sites Report No. UCB/EERC-72/12, Earthquake Engineering Research Center, University of California, Berkeley
- Sharma B, Chopra S, Sutar AK, Bansal BK (2013) Estimation of strong ground motion from a great earthquake Mw 8.5 in central seismic gap region, Himalaya (India) using empirical Green's function technique. *Pure and Appl Geophys* 170(12):2127–2138
- Shyu JH, Chen CF, Wu YM (2016) Seismotectonic characteristics of the northernmost Longitudinal Valley, eastern Taiwan: Structural development of a vanishing suture. *Tectonophysics* 692:295–308
- Smoczyk GM, Hayes GP, Hamburger MW, Benz HM, Villaseñor AH, Furlong KP (2013) Seismicity of the Earth 1900–2012 Philippine Sea plate and vicinity (No. 2010–1083-M). US Geological Survey.
- Sokolov V, Kuo-Liang W, Miksat J, Wenzel F, Chen CT (2009) Analysis of Taipei basin response for earthquakes of various depths and locations using empirical data. *TAO: Terrestrial, Atmospheric and Oceanic Sci*, 20(5), 6.
- Tagiguchi M, Asano K, Iwata T (2011) The comparison of source models of repeating subduction-zone earthquakes estimated using broadband strong motion records. *Zisin (Journal of the Seismological Society of Japan. 2nd ser.)*, 63(4), 223–242.
- Toro GR, McGuire RK (1987) An investigation into earthquake ground motion characteristics in eastern North America. *Bull Seismol Soc Am* 77(2):468–489
- U.S. Geological Survey (2019). Earthquake Lists, Maps, and Statistics, accessed April 18, 2019 at URL <https://www.usgs.gov/natural-hazards/earthquake-hazards/lists-maps-and-statistics>.
- Wells DL, Coppersmith KJ (1994) New empirical relationships among magnitude, rupture length, rupture width, rupture area, and surface displacement. *Bull Seismol Soc Am* 84(4):974–1002
- Wen YY, Wen S, Lee YH, Ching KE (2019) The kinematic source analysis for 2018  $M_w$  6.4 Hualien. *Taiwan Earthquake Terr Atmos Ocean Sci* 30:377–387
- Wu FT, Liang WT, Lee JC, Benz H, Villasenor A (2009) A model for the termination of the Ryukyu subduction zone against Taiwan: A junction of collision, subduction/separation, and subduction boundaries. *J Geophys Res: Solid Earth*, 114(B7).
- Zeng Y, Anderson JG, Yu G (1994) A composite source model for computing realistic synthetic strong ground motions. *Geophys Res Lett* 21(8):725–728

Springer Nature or its licensor holds exclusive rights to this article under a publishing agreement with the author(s) or other rightsholder(s); author self-archiving of the accepted manuscript version of this article is solely governed by the terms of such publishing agreement and applicable law.